An Enhanced Approach to Imaging the Indoor Environment using WiFi RSSI Measurements

Amartansh Dubey, Pranay Sood, Jehiel Santos, Dingfei Ma, *Student Members, IEEE*, Chi-Yuk Chiu, *Senior Member, IEEE* and Ross Murch, *Fellow, IEEE*

Abstract—Indoor device-free localization (DFL) using radio frequency (RF) signals has many important applications including navigation, security and inventory control. One of the most common approaches to indoor DFL is Radio Tomographic Imaging (RTI) which is based on line-of-sight (LOS) signal models and often utilizes WiFi signals. In this work, we propose a new extended Rytov phaseless imaging (xRPI) technique for indoor imaging that can image the shape and refractive index of objects in the indoor environment using WiFi RSSI measurements. Estimation of refractive index can be used to distinguish different object types within the environment. In addition, methods to reduce the number of RSSI measurements required for indoor imaging are also developed and these use a strong spatial sparsity constraint which directly arises from imaging change in the environment. Theoretical developments that support these contributions include increasing the validity range of the Rytov approximation by using a high frequency approximation to the total field, incorporating temporal background subtraction, incorporating electric field sensing using directional antennas, and utilization of Fresnel zones. Experimental demonstration of the performance of the proposed method is provided using a 20 node WiFi system. The results show that xRPI provides considerable improvement over RTI in accurately imaging shapes of different objects in an indoor environment. It also provides an estimate of the refractive index which is not possible with RTI or other Wi-Fi based indoor imaging techniques.

Index Terms—Device-free localization, Inverse Scattering, Indoor Imaging, Sparse Optimization, See-Through-Wall imaging

I. INTRODUCTION

Indoor localization, tracking and imaging using radio frequency (RF) signals has many important applications including navigation, security and inventory control. The techniques can be categorized into device-based active localization [1]–[3] and device-free localization (DFL) [4]–[34]. DFL methods do not require any active device to be included with the target and are therefore more convenient than device-based localization. DFL methods based on RF also provide a non-intrusive approach that can see through obstacles such as walls [32]–[34]. On the other hand, DFL methods relying on infrared (Kinect [11]), Laser (LiDAR [12]), and visible light [14], [35] signals are also useful but fail if the target is occluded or in darkness.

Our interest, in this work, is in RF based DFL techniques because they can handle targets that are occluded.

There has been extensive research performed on RF based DFL methods using WiFi. This includes passive coherent localization [4]–[7], machine learning "fingerprint" methods [15]–[19] and several advanced MIMO systems which utilize multipath scattering caused by moving objects to estimate their location while adaptively canceling the scattering from clutter [8]–[10], [36], [37]. These techniques can provide good localization accuracy. However, it is important to note the difference between *localization* and *imaging*. Localization refers to the tracking of the centroid of a moving target whereas imaging is a more intricate task which also requires estimation of shape, size and electrical properties (such as refractive index) of the target. The field of indoor imaging using WiFi signals is relatively new as compared to DFL.

The research fields which are often associated with indoor RF imaging problems are in the electromagnetic and mobile computing communities. The electromagnetic community approaches the imaging problem by formally solving inverse scattering problems that model wave phenomena including diffraction, scattering and reflection [38]–[40]. This provides good fidelity reconstructions and has been commercially deployed in a wide range of applications such as medical imaging [41], security checks [42], oil and gas exploration [43], and nondestructive testing [44]. However, the approach usually requires a controlled environment with a large number of precise measurements to accurately scan the domain of interest (DOI) and the models used are computationally intensive in general. Furthermore, the scale of the imaging domain is often restricted to a few wavelengths in each dimension to reduce the computational load of the problem. For these reasons, there has been limited work on applying inverse scattering methods to indoor imaging using WiFi signals in the electromagnetic community.

The mobile computing community approaches the indoor RF imaging problem through a different perspective and is based on RF shadowing effects. The target's location is estimated by modeling the shadowing caused by the object along the LOS path while ignoring multipath effects and is termed Radio Tomographic Imaging (RTI). RTI has been extensively researched in the last decade [20]–[29]. The measurement system for RTI consists of a wireless sensor network and multiple transceiver nodes that are placed around the DOI. The attenuation caused by the target along various LOS wireless links (between the nodes) provides an estimate of its size and location. Localization in RTI is generally limited

to localization of very high refractive index targets such as the human body [20]–[29]. Because RTI relies on shadowing caused by objects, it is not effective for imaging objects with low refractive index [45].

A. Motivation and Contributions

The motivation for this work is to enhance RTI by improving the range and types of objects that can be located as well as estimating an object's shape and refractive index. Refractive index estimation could be useful for obtaining information about the materials imaged in the indoor environment. For example, it would allow human movement to be distinguished from movement of furniture or inventory [46]–[48]. Refractive index estimation is also used in other fields such as optical computed tomography and microwave imaging for distinguishing material types [41], [42], [47]–[50].

To achieve our goals, our approach is to develop imaging techniques which are a hybrid of both the inverse scattering approach and the more straightforward RTI framework. In particular, we develop a new extended Rytov phaseless imaging technique (xRPI) that enhances the performance of RTI without significantly increasing measurements or computational complexity. Previous research along these lines includes Robotic Through-Wall Imaging (RTWI) [30]–[32]. RTWI operates at the intersection of LOS models such as RTI but uses an approximate inverse scattering method known as the Rytov approximation. Unlike RTI, RTWI can also provide shape reconstruction of the target [30]. A key difference between RTI and RTWI is in the measurement system. RTWI uses two robots with high gain antennas (15 dBi). During measurement, the robots are located outside the DOI at diametrically opposite sides and moved in parallel to collect transmission measurements through the DOI and along the direction of high gain. Good results were obtained but limitations include the requirement for specialized measurement equipment and a potentially lengthy measurement process in which the environment should be stationary [30]. More details about RTWI can be found in [30], [32]. Furthermore, neither RTI nor RTWI do not provide any estimates for refractive index and only provide binary images showing the presence or absence of the target.

In this paper, the key contributions include:
1) Development of a new extended Rytov phaseless imaging technique (xRPI) which improves the conventional formulation of RTI. xRPI provides significant improvement in the reconstruction quality and also provides estimates of refractive index using only WiFi RSSI measurements, while maintaining the straightforward measurement process of RTI.
2) Exploitation of temporal sparsity in the imaging environment to reduce the required number of measurements and to enhance the reconstruction of the temporal change in the DOI by removing distortion due to background clutter.
3) Provide experimental results using RSSI measurements from WiFi nodes to demonstrate the technique in a variety of indoor environments. We demonstrate experimentally that we can distinguish between different objects (having

different refractive index) in the DOI even in an occluded office environment.

Overall, the proposed xRPI technique not only outperforms RTI in shape reconstruction quality, but also provides approximate estimates of refractive index, which to the best of our knowledge, is not possible with RTI or other Wi-Fi based indoor imaging methods.

In the development of xRPI, we integrated the following theoretical extensions together to significantly improve performance compared to RTI:
1) Extended the validity range of the Rytov approximation by including a ray-based high frequency approximation to the total field
2) Included temporal background subtraction in the formulation to remove clutter and enhance reconstruction quality
3) Explicitly incorporated electric field sensing using directional antennas in the extended Rytov formulation
4) Formulated the extensions for use with phaseless or receive signal strength indicator (RSSI) measurements.
5) Enhanced reconstruction quality in the extended Rytov formulation by leveraging Fresnel zones

The contributions are predicated on realizing that the indoor environment is often sparse, and different from conventional inverse scattering scenarios. In particular, it is mainly free-space with distinct objects such as walls, furniture and people. Furthermore, the indoor environment is predominately stationary and time variations primarily occur due to the movement of people or objects that are distinct from indoor structures such as walls. Therefore estimating temporal change allows us to include a very strong sparsity constraint which we refer to here as temporal sparsity.

B. Organization and Notation

In Section II, we describe the configuration of our indoor imaging problem and introduce the background for its formulation. In Section III, we formulate the inverse problem considered in this paper and introduce the new extended Rytov phaseless imaging method (xRPI). In Section IV, the approach to numerically solve the resulting model is given. Section V provides a step-by-step implementation summary of xRPI followed by experimental results in Section VI.

In the remainder of this paper lower and upper case boldfaced letters are used to represent vectors and matrices respectively. Italic letters are used to represent scalars such as elements of vectors.

II. PROBLEM FORMULATION

A. Configuration

Consider a DOI, consisting of an area of dimensions $d_x \times d_y$ within a single floor of a building, and denoted as $\mathcal{D} \subset \mathbb{R}^2$ in Fig. 1. The wireless nodes (transceivers) are placed at the boundary (denoted as $\mathcal{B} \subset \mathbb{R}^2$) of the DOI (see Fig. 1) and can transmit and receive signals to acquire RSSI measurements of the links between each node. The total number of nodes is M and therefore the total number of unique wireless links is $L = M(M-1)/2$. The unique L links do not include
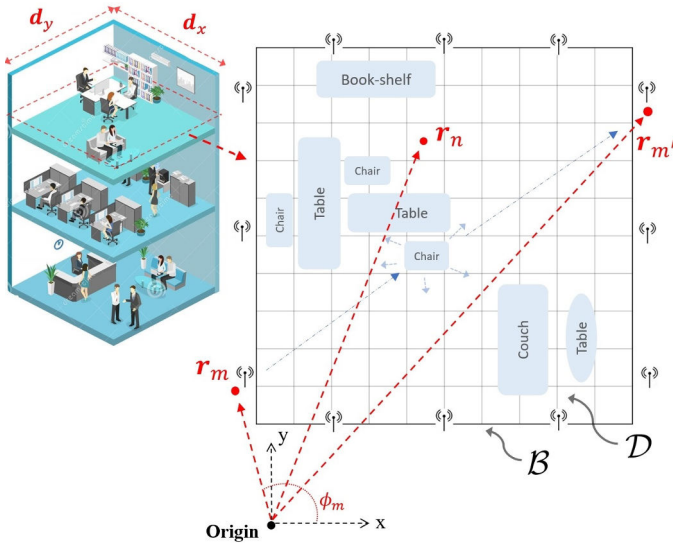
Fig. 1: The DOI with wireless nodes (transceivers) at its boundaries $\mathcal{B}$. The position vectors of the transmitter m and receiver m' are $\mathbf{r}_m \in \mathcal{B}$ and $\mathbf{r}_{m'} \in \mathcal{B}$ respectively. The corresponding polar coordinates are (r_m, ϕ_m) and $(r_{m'}, \phi_{m'})$ respectively. An arbitrary point in the DOI is denoted as $\mathbf{r}_n \in \mathcal{D}$ with polar coordinates (r_n, ϕ_n). All coordinates are defined with respect to the origin as shown at the bottom with x- and y-axis.

the reciprocal links or self measurements since nodes cannot usually transmit and receive at the same time.

The location of the mth measurement node is denoted by $\mathbf{r}_m \in \mathcal{B}$ (see Fig. 1) and in polar coordinates is written as (r_m, ϕ_m). The link between transmitting node m (located at $\mathbf{r}_m$) and receiving node m' (located at $\mathbf{r}_{m'}$) is written $l_{m,m'}$. The scripts m and m' are used throughout the remainder of this work to denote the transmitter and receiver respectively on all relevant quantities.

The nodes are located at height d_h from the floor and have fitted to them a vertically polarized directive antenna. The antennas radiate inwards towards the DOI. Because the antennas are orientated vertically, electromagnetic radiation is vertically polarized and this is often referred to as transverse magnetic (TM) in inverse scattering contexts. Further details of the measurement system are provided later in section VI. The nodes consist of standard WiFi transceivers using directive antennas with gain 6.6 dBi at $d_h = 1.2$ m.

The environment is approximated as a two-dimensional (2D) electromagnetic problem where the DOI can be considered a 2D planar cross-section through the single floor at height d_h. The 2D approximation is predicated on scattering from the floor and ceiling being small so that scattering is predominately from objects in the DOI cross-section. This is achieved by the directive antennas at the nodes which focus radiation to the 2D cross-section and reduce it in the direction of the floor and ceiling. In particular, fading caused by reflections from the ceiling and floor will be dramatically reduced in the DOI. While the coverage area of the WiFi system will be much larger than the DOI, restricting the DOI to areas less than 5×5 m^2 will ensure that the 2D approximation remains valid and fading is not a significant issue.

We use Wi-Fi signals with frequency $f_0 = 2.4$ GHz, for which wavelength $\lambda_0 = 12.5$ cm (and wavenumber $k_0 =$

$\omega\sqrt{\epsilon_0\mu_0} = 50.265$ m^{-1}, where ϵ_0 and μ_0 are free space permittivity and permeability respectively). The wavelength involved is smaller than the objects of interest in the scenario we are considering. Therefore ray tracing models based on ray tracing approximations such as the Uniform Theory of Diffraction (UTD) are well accepted to provide good predictions of electromagnetic scattering [39], [51].

The DOI has a homogeneous background medium of air (ϵ_0, μ_0) and is embedded with scatterers (such as furniture and people) having relative permittivity ϵ_r at 2.4 GHz. This work considers scatterers to be non-magnetic in which relative permeability throughout the DOI is $\mu_r = \mu_0$. Therefore, we characterize the permittivity profile of the DOI using refractive index $\nu(\mathbf{r}) = \sqrt{\epsilon_r(\mathbf{r})}$.

Time variation of $\nu(\mathbf{r})$ (or its temporal change) is an important focus of this work. The temporal change in the refractive index profile (such as movement of people and objects) considered in our problem is slow compared to the wave speed and therefore when we include time in $\nu(\mathbf{r})$, we write it as a superscript as $\nu^t(\mathbf{r})$ rather than including it inside the argument. The time variation of $\nu^t(\mathbf{r})$ models the movement of objects and people within the DOI. For a time step Δt, the resultant change in refractive index is written as

$$\Delta\nu(\mathbf{r}) = \nu^{t+\Delta t}(\mathbf{r}) - \nu^t(\mathbf{r}). \tag{1}$$

and quantifies the concept of temporal change. The time increment Δt used for this method can be set to any value over which changes are to be detected. It could be set from seconds to days depending on the specific application. The temporal difference, no matter what the time scale, provides an estimate of the change of the environment and can be a useful estimate of the movement of people at short time scales, to the removal of furniture over longer time scales.

The DOI (of dimension $d_x \times d_y$) is discretized into N rectangular grids each with dimensions $\Delta d_x \times \Delta d_y$ (and area $\Delta a = \Delta d_x \times \Delta d_y$). For inverse scattering problems, the size of the grid should be significantly smaller than the incident wavelength ($\Delta d_x, \Delta d_y \ll \lambda_0$) [39]. The location of the nth grid is denoted as $\mathbf{r}_n$ (see Fig. 1) and in polar coordinates it is written as (r_n, ϕ_n).

Our imaging goal is to estimate change in refractive index for all N grids and hence generate a 2D refractive index $\Delta\nu(\mathbf{r}_n)$ image of change from t to $t + \Delta t$. In essence, we aim to solve for the unknown refractive index at N grid points with $L = M(M-1)/2$ measurements. This problem is clearly under determined ($N \gg L$) and is solvable by realizing that $\Delta\nu(\mathbf{r}_n)$ will be spatially sparse so that regularization can be utilized. This is discussed in detail in the following sections.

B. Formulation

Fig. 2 is an extension to Fig. 1 and defines the geometry used in the following formulation. Node m generates a vertically polarized time harmonic electric field $E_m^i(\mathbf{r}_n)$ that is incident on locations $\mathbf{r}_n$ in the DOI. The incident field interacts with objects in the DOI creating a scattered field $E_m^s(\mathbf{r}_n)$. The total electric field $E_m(\mathbf{r}_n)$ at any point in the DOI is therefore the sum of both parts and written as

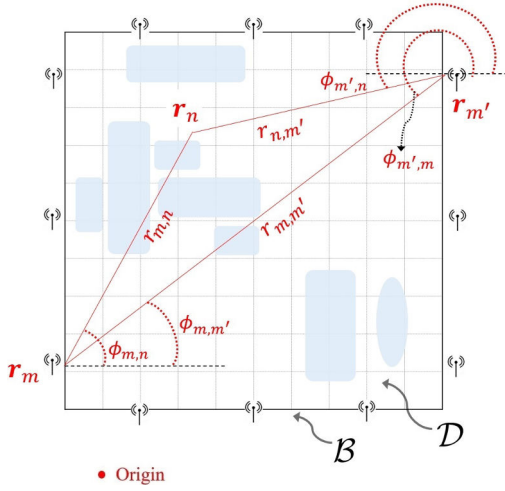$$E_m(\mathbf{r}_n) = E_m^i(\mathbf{r}_n) + E_m^s(\mathbf{r}_n). \tag{2}$$

Fig. 2: Details of the geometry used in the formulation (extension to Fig. 1). Distances $r_{m,n}$ and $r_{m,m'}$ are the distances between the mth transmitter node and the grid point $\mathbf{r}_n$ and receiver $\mathbf{r}_{m'}$ respectively. Angle $\phi_{m,n}$ and $\phi_{m,m'}$ are consequently defined as the angles at the mth transmitter node to the grid point $\mathbf{r}_n$ and receiver $\mathbf{r}_{m'}$ respectively. Definitions for the distances and angles from the m'^{th} receiver node follow the same approach.

The field received at node m' (transmitted by node m) can be expressed using the Lippmann-Schwinger equation [39] and written as

$$
\begin{aligned}
E_m(\mathbf{r}_{m'}) &= E_m^i(\mathbf{r}_{m'}) + E_m^s(\mathbf{r}_{m'}) \\
&= E_m^i(\mathbf{r}_{m'}) + (-j)\omega\mu_0 \sum_{\forall n|\mathbf{r}_n \in \mathcal{D}} g(k_0 r_{n,m'}) J_m(\mathbf{r}_n)\Delta a.
\end{aligned}
\tag{3}
$$

where $r_{n,m'} = |\mathbf{r}_{m'} - \mathbf{r}_n|$ (see Fig. 2) and $g(k_0 r_{n,m'})$ is the standard Green's function (in 2D it is written as a Hankel function as $\frac{j}{4}H_0^{(1)}(k_0 r_{n,m'})$) and $J_m(\mathbf{r}_n)$ is referred to as equivalent induced sources in the DOI and written as

$$
J_m(\mathbf{r}_n) = -j\omega\epsilon_0\big(\nu^2(\mathbf{r}_n) - 1\big)E_m(\mathbf{r}_n).
\tag{4}
$$

Equation (3) represents the summation of the scattered fields (from all N grids inside DOI) at the receiver m'. Note that the equivalent induced sources are proportional to the total electric field $E(\mathbf{r}_n)$ (consisting of both the scattered and incident fields at each grid) as well as the refractive index $\nu(\mathbf{r}_n)$.

The antenna far-field pattern of each of the nodes in the system are taken as identical and written as $F(\theta) = \sqrt{e_r D_0}E(\theta)$ where $E(\theta)$ denotes the normalized electric far-field antenna pattern (i.e. $|E(\theta)|_{\max} = 1$ with the maximum direction or main beam oriented to $\theta = 0°$). D_0 denotes directivity defined as

$$
D_0 = \frac{4\pi}{\int |E(\theta)|^2 \, \mathrm{d}\theta},
\tag{5}
$$

and e_r denotes the radiation efficiency of the antenna.

An antenna located on the mth node is oriented such that its main beam angle, denoted as θ_m, is normal to the measurement boundary $\mathcal{B}$ and pointing inwards to the DOI. For example, for nodes on the right vertical boundary in Fig. 2, $\theta_m = 180°$. Nodes at the corners of the DOI, are orientated along the diagonal of $\mathcal{B}$ so that $\theta_m = 45°, 135°, 225°, 315°$ for each corner respectively.

With the use of directional antennas, the incident field can be written as

$$
E_m^i(\mathbf{r}_n) = A_0 \ g(k_0 r_{m,n}) \cdot F(\phi_{m,n} - \theta_m),
\tag{6}
$$

where A_0 is the transmitted electric field amplitude, $r_{m,n} = |\mathbf{r}_n - \mathbf{r}_m|$ and $\phi_{m,n}$ is the angle from the mth node to the nth grid point as shown in Fig. 2. In this expression we have straightforwardly used the Green's function to represent an omni-directional radiating antenna which is modified by its product with the antenna pattern $F(\phi_{m,n} - \theta_m)$ to form the incident field at $\mathbf{r}_n$.

Referring to (3), the imaging or inverse problem is defined here as finding $\nu(\mathbf{r}_n)$ from measurements $E_m(\mathbf{r}_{m'})$ and knowledge of the incident field $E_m^i(\mathbf{r}_n)$. On the other hand the direct problem is defined here as finding the total electric field $E_m(\mathbf{r}_{m'})$ at the receiver given $E_m^i(\mathbf{r}_n)$ and $\nu(\mathbf{r}_n)$.

The inverse problem is considered more difficult to solve than the direct problem since both $\nu(\mathbf{r}_n)$ and $E_m(\mathbf{r}_n)$ are unknown in the DOI and have a non-linear relation with the measurements. Also, as discussed previously, the inverse problem considered is severely under-determined ($N \gg L$).

In the next section we provide a method to approximately, but efficiently solve for temporal changes in the refractive index profile $\Delta\nu(\mathbf{r}_n)$ using RSSI measurements at the nodes.

III. EXTENDED RYTOV PHASELESS IMAGING

To avoid the ill-posedness and non-linearity of the inverse problem in (3), linear approximations such as the Born and Rytov approximations are often invoked [39]–[41], [49], [52]–[55]. The use of these approximations is usually limited to situations where refractive index has small deviations from unity (Born approximation) and the less strict form, as small deviations from unity per wavelength (Rytov approximation) [39]–[41], [50], [52]. These limitations prevent the approximations from being used widely and they are not applicable to indoor imaging for example. Therefore, extensions to the approximations have been attempted [40], [50] to meet specific limitations and applications but they remain unsuitable for the particular challenges of indoor imaging.

In this work, we extend the Rytov approximation for use in indoor imaging. In particular, we enhance the validity range of the Rytov approximation by including a ray-based high frequency approximation to the total field [40], [54]. We also incorporate temporal background subtraction, directional antennas, phaseless measurements, and Fresnel zones. Taken together these extensions dramatically enhance the performance of RTI allowing shape and refractive index estimation to be performed in indoor environments.

The total field at any point $\mathbf{r}_n$ due to node m transmitting can also be expressed as [39], [52], [53]

$$
E_m(\mathbf{r}_n) = e^{-jk_0(S_m^i(\mathbf{r}_n)+S_m^s(\mathbf{r}_n))},
\tag{7}
$$

where $S_m^s(\mathbf{r}_n)$ and $S_m^i(\mathbf{r}_n)$ can be considered the complex wavefronts of the scattered and incident fields in the DOI so that $E_m^i(\mathbf{r}_n) = e^{-jk_0 S_m^i(\mathbf{r}_n)}$. The real and imaginary parts of $(S_m^i(\mathbf{r}_n) + S_m^s(\mathbf{r}_n))$ incorporate wavefront curvature and amplitude variations respectively.

The Rytov transformation [39], [52], [53] can then be invoked to transform the total field into the logarithmic domain as

$$\tilde{E}_m(\mathbf{r}_n) = \ln\left[\frac{E_m(\mathbf{r}_n)}{E_m^i(\mathbf{r}_n)}\right] \cdot E_m^i(\mathbf{r}_n)$$
$$= -jk_0 S_m^s(\mathbf{r}_n)e^{-jk_0 S_m^i(\mathbf{r}_n)}. \tag{8}$$

Rewriting (3) in terms of $\tilde{E}_m(\mathbf{r}_n)$ provides [39], [52], [53],

$$\tilde{E}_m(\mathbf{r}_{m'}) = -j\omega\mu_0 \sum_{\forall n|\mathbf{r}_n\in\mathcal{D}} g(k_0 r_{n,m'})\tilde{J}_m(\mathbf{r}_n)\Delta a, \tag{9}$$

where the induced source term $\tilde{J}_m(\mathbf{r}_n)$ is

$$\tilde{J}_m(\mathbf{r}_n) = -j\omega\epsilon_0\left[(\nu^2(\mathbf{r}_n)-1)-\nabla S_m^s(\mathbf{r}_n)\cdot\nabla S_m^s(\mathbf{r}_n)\right]E_m^i(\mathbf{r}_n). \tag{10}$$

The conventional Rytov approximation neglects the term $\nabla S_m^s(\mathbf{r}_n)\cdot\nabla S_m^s(\mathbf{r}_n)$ to simplify the equations [52] and arrive at the standard Rytov formulation [39], [40].

In this work, we extend the Rytov approximation by utilizing a previous suggestion [53], [56] to approximate the term $\nabla S_m^s(\mathbf{r}_n)\cdot\nabla S_m^s(\mathbf{r}_n)$ by using its ray path. It is particularly suitable in our configuration because the directive antennas and environment considered restrict the ray paths to predominately lie in the direct transmission or LOS path.

The extension to the Rytov approximation involves invoking a ray-based high frequency approximation to the total field [52]–[54], [56] as

$$E_m(\mathbf{r}_n) = \nu(\mathbf{r}_n)^{1/2}e^{-jk_0\int_{\mathbf{l}_{m,n}}\nu(\mathbf{r}_n)ds}, \tag{11}$$

where $\mathbf{l}_{m,n}$ denotes the ray path from the transmitter at node m passing through point $\mathbf{r}_n$. By using the assumption that the paths do not significantly deviate from LOS, we can approximate the actual ray path $\mathbf{l}_{m,n}$ by the straight ray path of the incident field. The unit direction vector of the ray path of the incident field at point $\mathbf{r}_n$ can be written as $\hat{k}_{m,n} = (\sin(\phi_{m,n}),\cos(\phi_{m,n}))^T$ [53], [56] so that we can express the term $\nabla S_m^s(\mathbf{r}_n)\cdot\nabla S_m^s(\mathbf{r}_n)$ as

$$\nabla S_m^s(\mathbf{r}_n)\cdot\nabla S_m^s(\mathbf{r}_n) \approx \left[\nu^2(\mathbf{r}_n)+1-2\nu(\mathbf{r}_n)\right]$$
$$+\left[\frac{j}{2k_0}(\nu(\mathbf{r}_n)-1)\frac{\partial\ln[\nu(\mathbf{r}_n)]}{\partial\hat{k}_{m,n}}+\right.$$
$$\left.\frac{1}{4k_0^2}(\nabla\ln[\nu(\mathbf{r}_n)])\cdot(\nabla\ln[\nu(\mathbf{r}_n)])\right]. \tag{12}$$

For paths with up to 20° deviation from LOS path, the error in approximation is less than 6% [53], [56]. This formulation is therefore particularly suited to indoor imaging scenarios where we predominantly rely on LOS paths. Furthermore, because k_0 in our imaging problem is large ($k_0 = 50.265$ m^{-1} for 2.4 GHz), we neglect terms in (12) having k_0 in the denominator. Hence (12) can be approximated as,

$$\nabla S_m^s(\mathbf{r}_n)\cdot\nabla S_m^s(\mathbf{r}_n) \approx \left[\nu(\mathbf{r}_n)^2+1-2\nu(\mathbf{r}_n)\right]. \tag{13}$$

On substituting $\nabla S_m^s(\mathbf{r}_n)\cdot\nabla S_m^s(\mathbf{r}_n)$ from (13) to (10), we obtain the induced source term for the extended Rytov approximation as,

$$\tilde{J}_m(\mathbf{r}_n) = -j2\omega\epsilon_0\left[\nu(\mathbf{r}_n)-1\right]E^i(\mathbf{r}_n). \tag{14}$$

Replacing $\tilde{J}_m$ in the Rytov approximation (9) provides the extended Rytov approximation as,

$$\tilde{E}_m(\mathbf{r}_{m'}) = -j\omega\mu_0 \sum_{\forall n|\mathbf{r}_n\in\mathcal{D}} g(k_0 r_{n,m'})\tilde{J}_m(\mathbf{r}_n)\Delta a$$
$$= k_0^2 \sum_{\forall n|\mathbf{r}_n\in\mathcal{D}} g(k_0 r_{n,m'})\chi(\mathbf{r}_n)E_m^i(\mathbf{r}_n)\Delta a, \tag{15}$$

where, $\chi(\mathbf{r}_n) = 2(\nu(\mathbf{r}_n)-1)$ is the contrast in the refractive index profile with respect to free space.

The key difference between the Rytov (9) and extended Rytov approximation (15) is that the term $\frac{1}{2}(\nu^2(\mathbf{r}_n)-1)$ is replaced with $(\nu(\mathbf{r}_n)-1)$. This agrees with physical intuition that the incremental phase along a path is related to $(\nu(\mathbf{r}_n)-1)$ rather than $\frac{1}{2}(\nu^2(\mathbf{r}_n)-1)$ as shown by (11). In practice, the differences are minor for small refractive indices but become significant if larger refractive indices are considered as in indoor imaging.

The importance of (15) is that it establishes a straight-forward linear relation between the unknown $\chi(\mathbf{r}_n)$ and the measured quantities $\tilde{E}_m(\mathbf{r}_{m'})$. While there are constraints that limit the range of validity of (15) [53], [56], in the next sections we describe methods that can increase the range of validity by utilizing temporal sparsity, incorporating directive antennas at the receiver and using Fresnel zones to restrict to transmission measurements.

A. Temporal Background Subtraction: Temporal Sparsity

Using (15) we can now focus on imaging change in the indoor environment. Two important observations need to be noted for imaging change. The first is that changes in the indoor environment are usually minor compared to the background scatterers consisting of walls and furniture. We can therefore impose a strong sparsity constraint on the change. We refer to this as temporal sparsity. The second key observation is that we can also expect to significantly enhance the performance of the reconstruction obtained using (15). This is because the stationary background objects will exhibit scattering that will be significant and violate the assumptions of the extended Rytov approximation. However these objects will usually be spatially separate and distinct from the moving or moved objects. This implies that scattering or interaction between the moving and stationary objects will usually not dominate the wave phenomena. Therefore subtracting out the stationary component will leave behind the signal predominately relating only to those moving objects. This part of the scattering will better satisfy the conditions of the extended Rytov approximation and therefore imaging change will be significantly enhanced as compared to attempting to image the background as well.

Because (15) is linear, it is straightforward to formulate for temporal change. Consider an initial time instant t_0 at which the refractive index profile of DOI is characterized by $\chi^{t_0}(\mathbf{r}_n) = 2(\nu^{t_0}(\mathbf{r}_n) - 1)$. In the next time frame $t_0 + \Delta t$, the DOI changes to $\chi^{t_0+\Delta t}(\mathbf{r}_n) = 2(\nu^{t_0+\Delta t}(\mathbf{r}_n) - 1)$ so that $\Delta\chi = \chi^{t_0+\Delta t}(\mathbf{r}_n) - \chi^{t_0}(\mathbf{r}_n) = 2\Delta\nu(\mathbf{r}_n)$. Applying (15) for both time frames provides an equation for $\Delta\chi$ as,

$$\Delta \tilde{E}_m(\mathbf{r}_{m'}) = k_0^2 \sum_{\forall n|\mathbf{r}_n \in \mathcal{D}} g(k_0 r_{n,m'})\Delta\chi(\mathbf{r}_n)E_m^i(\mathbf{r}_n)\Delta a, \quad (16)$$

where, using (8), $\Delta\tilde{E}_m(\mathbf{r}_{m'})$ is written as

$$\Delta\tilde{E}_m(\mathbf{r}_{m'}) = \tilde{E}_m^{t_0+\Delta t}(\mathbf{r}_{m'}) - \tilde{E}_m^{t_0}(\mathbf{r}_{m'})$$
$$= E_m^i(\mathbf{r}_{m'}) \cdot \ln\left[\frac{E_m^{t_0+\Delta t}(\mathbf{r}_{m'})}{E_m^{t_0}(\mathbf{r}_{m'})}\right]. \quad (17)$$

Noting (17) and dividing (16) by $E_m^i(\mathbf{r}_{m'})$, we can obtain a more useful form in terms of directly measurable fields as

$$\ln\left[\frac{E_m^{t_0+\Delta t}(\mathbf{r}_{m'})}{E_m^{t_0}(\mathbf{r}_{m'})}\right] = k_0^2 \cdot \left[\sum_{\forall n|\mathbf{r}_n \in \mathcal{D}} \psi^{(m',n)}\Delta\chi(\mathbf{r}_n)\right], \quad (18)$$

where $\psi_m^{(m',n)}$ is the kernel weight between the transmitter at node m, the nth grid and the receiver at node m' and expressed as

$$\psi_m^{(m',n)} = \frac{\sum_{\forall n|\mathbf{r}_n \in \mathcal{D}} g(k_0 r_{n,m'})E_m^i(\mathbf{r}_n)\Delta a}{E_m^i(\mathbf{r}_{m'})}. \quad (19)$$

We show later that (18) can be conveniently expressed as RSSI measurements in dB.

While the approach (18) is straightforward to apply, its effect will be significant on reconstruction quality when the moving objects within the indoor environment do not interact significantly with the background. Subtracting the background stationary component, under this assumption, leaves only those fields associated with scattering from the moving objects. Since these are limited in size we can expect the extended Rytov approximation to perform more satisfactorily with imaging change. This effect has been shown in 1D previously [49] but will be even more significant in 2D due to the more intricate environment and scattering. Therefore, (18) can have potential to image changes even in highly cluttered DOI as we shall show later.

B. Electric Field Sensing using Directive Antennas

The electric field at the receiver $E_m(\mathbf{r}_{m'})$ must be appropriately sensed and converted to a voltage and this can be performed by an antenna. This step is often neglected in imaging formulations because the antennas are assumed to be omnidirectional. In this work, due to the intricate environment, we use directive antennas at the receivers. Directivity plays a key role in the performance of our formulation because it restricts the fields to predominately lie in the direct transmission or LOS path between the transmitter and receiver and helps meet the validity conditions of our extended Rytov approximations such as (11).

The received voltage at node m' due to the field arriving at angle $\phi_{m',n}$ (see Fig. 2) to the receiver can be written as [57],

$$V_m(\mathbf{r}_{m'}) = E_m(r_{m',n}, \phi_{m',n})h(\phi_{m',n}), \quad (20)$$

where $h(\phi_{m',n})$ is known as the antenna height (all nodes use the same antenna type) and given by [57],

$$h(\phi_{m',n}) = \frac{\lambda}{j}\sqrt{\frac{R}{\pi Z_\eta}}F(\phi_{m',n} - \theta_{m'}), \quad (21)$$

where R is the input resistance of the antenna, $Z_\eta = 377\ \Omega$ is the impedance of free space and $F(\cdot)$, and $\theta_{m'}$ are antenna parameters defined previously (see (5) and (6)). This is straightforwardly incorporated into the formulation (3) by applying (20) to express the total received field $E_m(\mathbf{r}_{m'})$ in terms of received voltage $V_m(\mathbf{r}_{m'})$ as

$$V_m(\mathbf{r}_{m'}) = h(\phi_{m',m})E_m^i(\mathbf{r}_{m'})$$
$$+ (-j)\omega\mu_0 \sum_{\forall n|\mathbf{r}_n \in \mathcal{D}} h(\phi_{m',n})g(k_0 r_{n,m'})\tilde{J}_m(\mathbf{r}_n)\Delta a. \quad (22)$$

Therefore, by incorporating (20) and (21) in the Lippmann-Schwinger equation (3), we are able to include receiver directivity for both LOS as well as scattered wave paths. Following the approach in (22) and updating the formulations (9), (15), (18) and (19) to include the antenna heights, the formulation for received voltage can be straightforwardly obtained by modifying the sensitivity kernel $\psi_m^{(m',n)}$ in (19) as

$$\psi_m^{(m',n)} = \frac{\sum_{\forall n|\mathbf{r}_n \in \mathcal{D}} h(\phi_{m',n})g(k_0 r_{n,m'})E_m^i(\mathbf{r}_n)\Delta a}{h(\phi_{m',m})E_m^i(\mathbf{r}_{m'})}. \quad (23)$$

Using (18) with (23) we obtain

$$\ln\left[\frac{V_m^{t_0+\Delta t}(\mathbf{r}_{m'})}{V_m^{t_0}(\mathbf{r}_{m'})}\right] = k_0^2 \cdot \left[\sum_{\forall n|\mathbf{r}_n \in \mathcal{D}} \psi_m^{(m',n)}\Delta\chi(\mathbf{r}_n)\right]. \quad (24)$$

By explicitly writing the incident field ($E_m^i(\mathbf{r}_{m'})$ and $E_m^i(\mathbf{r}_n)$) in terms of directivity (see (6)) and using (21), $\psi_m^{(m',n)}$ can be expanded as,

$$\psi_m^{(m',n)} = \underbrace{\frac{g(k_0 r_{n,m'})g(k_0 r_{m,n})}{g(k_0 r_{m,m'})}}_{\text{Omnidirection fields}} \underbrace{\frac{F(\phi_{m',n} - \theta_{m'})F(\phi_{m,n} - \theta_m)}{F(\phi_{m',m} - \theta_{m'})F(\phi_{m,m'} - \theta_m)}}_{\text{Net Directional Gain}}\Delta a. \quad (25)$$

The second term in (25) represents the effect of directional transmit and receive antennas. The denominator is constant for a given $l_{m,m'}$ link while the numerator varies depending on the scattering point $\mathbf{r}_n$. In particular, the kernel will be greatest where the scattering point is close to the main beams of both antennas. If all the antennas were omnidirectional, the net directional gain term in (25) becomes unity and only the first omnidirectional term would remain as in conventional formulations. We can deduce that the directional antennas are effectively weighting the kernel for the paths that do not significantly deviate from LOS paths.

C. Phaseless form

It is important to consider measurement data which can be conveniently acquired. Therefore, in this work we formulate the inverse problem in terms of phaseless data such as RSSI. By using only RSSI measurements, there is no need for phase measurements or synchronization between the radio nodes and it simplifies the measurement process significantly. Furthermore, RSSI data is straightforwardly accessible from many common off-the-shelf WiFi boards (and other wireless systems such as Bluetooth and Zigbee). To formulate our

expressions in phaseless form we first write (24) in exponential form as,

$$\left[\frac{V_m^{t_0+\Delta t}(\mathbf{r}_{m'})}{V_m^{t_0}(\mathbf{r}_{m'})}\right] = \exp\left(k_0^2 \cdot \sum_{\forall n | \mathbf{r}_n \in \mathcal{D}} \psi_m^{(m',n)} \Delta\chi(\mathbf{r}_n)\right). \quad (26)$$

Multiplying (26) by its complex conjugate [32] and then taking log base 10 on both sides gives,

$$\Delta\mathcal{P}_m(\mathbf{r}_{m'})[\text{dB}] = 10 \log_{10} e^{2k_0^2} \cdot \text{Re}\left[\sum_{\forall n | \mathbf{r}_n \in \mathcal{D}} \psi_m^{(m',n)} \Delta\chi(\mathbf{r}_n)\right], \quad (27)$$

where $\Delta\mathcal{P}_m(\mathbf{r}_{m'})$ is change in received power (in dB) across Δt and written as

$$\Delta\mathcal{P}_m(\mathbf{r}_{m'})[\text{dB}] = 10 \log_{10}\left|\frac{V_m^{t_0+\Delta t}(\mathbf{r}_{m'})}{V_m^{t_0}(\mathbf{r}_{m'})}\right|^2. \quad (28)$$

Equation (27) linearly relates the change in RSSI (received power) (in dB) to the change in refractive index profile.

D. Fresnel Zone Sensitivity Constraint

To further focus our formulation towards direct transmission or LOS paths, we also impose a final additional constraint on the kernel. In particular, we only consider elements of the kernel that fall within the first Fresnel zone of the direct path between the transmitter m and receiver m'. This forces the reconstruction to only consider transmission paths rather than those that could have been reflected from objects and which our extended Rytov formulation cannot handle well. The first Fresnel zone contains most of the electromagnetic energy and in other work similar elliptical based regions have also been considered [55], [58]–[60]. The linear tomographic inversions of these approaches were shown to be more stable and accurate if the sensitivity kernel weights are constrained to the Fresnel zone [55], [58]–[60].
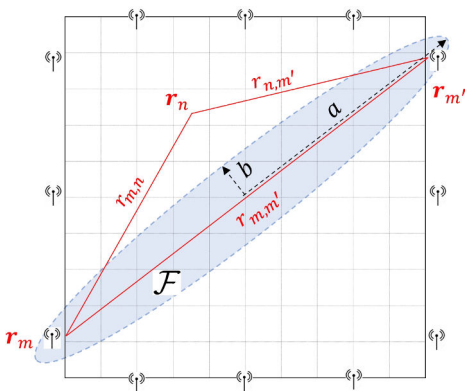

Fig. 3: Illustration of the first Fresnel zone (shaded ellipse) between the transmitter m and receiver m' nodes. The transmitter and receiver nodes are placed at the foci of the Fresnel zone elliptical region. The length of the elliptical semi-major and semi-minor axis and distance between its foci are a, b and $\mathbf{r}_{m,m'}$ respectively.

Fig. 3 illustrates the first Fresnel zone $\mathcal{F}$ (shaded elliptical region) with its foci at the transmitter m and receiver m'. The length of the elliptical semi-minor axis, semi-major axis and distance between its foci are denoted as b, a and $r_{m,m'}$ respectively. The maximum radius b (or semi-minor axis) of

the Fresnel zone $\mathcal{F}$ is a function of transmitted wavelength λ_0 and distance $r_{m,m'}$ and written as [61],

$$b = \sqrt{\frac{\lambda_0 \, r_{m,m'}}{4}}. \quad (29)$$

From the properties of the ellipse, we can express the semi-major axis a as

$$a = \sqrt{b^2 + \left(\frac{r_{m,m'}}{2}\right)^2} = \frac{1}{2}\sqrt{\lambda_0 r_{m,m'} + (r_{m,m'})^2}. \quad (30)$$

Any grid at location $\mathbf{r}_n$ with distance $r_{m,n}$ and $r_{n,m'}$ from two foci (m and m', see Fig. 2) can be classified as being within or outside the first Fresnel zone $\mathcal{F}$ using

$$\text{if } r_{m,n} + r_{n,m'} \le 2a = \sqrt{\lambda_0 r_{m,m'} + (r_{m,m'})^2} \quad\Rightarrow\quad \mathbf{r}_n \in \mathcal{F} \quad (31a)$$

$$\text{if } r_{m,n} + r_{n,m'} > 2a = \sqrt{\lambda_0 r_{m,m'} + (r_{m,m'})^2} \quad\Rightarrow\quad \mathbf{r}_n \notin \mathcal{F} \quad (31b)$$

To set the sensitivity kernel weights outside the first Fresnel zone to zero, we introduce an indicator function $\mathcal{I}(r_{m,n}, r_{n,m'}, r_{m,m'})$ in (25) as

$$\tilde{\psi}_m^{(m',n)} = \underbrace{\mathcal{I}(r_{m,n}, r_{n,m'}, r_{m,m'})}_{\text{Fresnel Constraint}} \cdot \underbrace{\psi_m^{(m',n)}}_{\text{kernel weights from (25)}}, \quad (32)$$

where,

$$\mathcal{I} = \begin{cases} 1 & \text{if } r_{m,n} + r_{n,m'} \le \sqrt{\lambda_0 r_{m,m'} + (r_{m,m'})^2} \\ 0 & \text{otherwise.} \end{cases} \quad (33)$$

Replacing $\psi_m^{(m',n)}$ with $\tilde{\psi}_m^{(m',n)}$ in (27) gives the final form of our proposed framework as

$$\Delta\mathcal{P}_m(\mathbf{r}_{m'})[\text{dB}] = 10 \log_{10} e^{2k_0^2} \cdot \text{Re}\left[\sum_{\forall n | \mathbf{r}_n \in \mathcal{D}} \tilde{\psi}_m^{(m',n)} \Delta\chi(\mathbf{r}_n)\right]. \quad (34)$$

Solving (34) provides image of changes in refractive index profile ($\Delta\nu(\mathbf{r}_n) = \Delta\chi(\mathbf{r}_n)/2$) using the change in RSSI values $\Delta\mathcal{P}_m(\mathbf{r}_{m'})[dB]$. Equation (34) is the final form of our proposed extended Rytov phaseless imaging method (xRPI)

IV. NUMERICAL SOLUTION

The combination of all the techniques we have described in the previous section provide us with our new extended Rytov phaseless imaging (xRPI) formulation, (34). It can image temporal change in the refractive index profile of an indoor region using WiFi RSSI measurements. However, (34) is severely under-determined ($N \gg L$) due to the large DOI in which there are a limited number of measurement nodes $N \gg M$. Therefore a solution using conventional least squares cannot be obtained. To overcome this issue, regularization is needed to impose prior information about the DOI. This again highlights the importance of temporal sparsity as previously discussed in Section III-A. Temporal sparsity is a very strong spatial sparsity constraint as spatial change (in duration Δt) within the indoor environment will be limited. Therefore temporal sparsity can be utilized as a regularization constraint in order to find a unique solution.

The first step towards regularizing using temporal sparsity is to define the complete formulation for all $L = M(M-1)/2$ wireless links. This is performed by stacking (34) with kernel (32) for all wireless links into a single equation as

$$\mathbf{y} = \boldsymbol{\Psi}\mathbf{x}, \tag{35}$$

where the measurement vector $\mathbf{y} \in \mathbb{R}^{L \times 1}$ has elements $y_l = \Delta\mathcal{P}_m(\mathbf{r}_{m'})$ [in dB] in which $l = m(m' - \text{ceil}(m/M))$ where $m = 1, 2, ..., M - 1$ and once m is selected, m' is given by $m' = 1 + \text{ceil}(m/M), ..., M$ (ceil denotes the ceiling or round up function). Note again that the L links considered do not include the reciprocal links or self measurements since nodes cannot usually transmit and receive at the same time. Correspondingly $\boldsymbol{\Psi} \in \mathbb{R}^{L \times N}$ contains elements with entries, $\boldsymbol{\Psi}_{l,n} = 10 \log_{10} e^{2k_0^2} \cdot \text{Re}(\tilde{\psi}_m^{(m',n)})$ (see (32)) where l is related to m and m' as above. Finally $\mathbf{x} \in \mathbb{R}^{N \times 1}$ is the unknown material vector with elements $\Delta\chi(\mathbf{r}_n)$ where $n = 1, 2, ...N$. The vector $\mathbf{x}$ should be highly sparse due to temporal sparsity.

In (35) we can impose temporal sparsity using several regularization techniques including Lasso, Tikhonov, and Total Variation (TV). Of these, TV has been the most successful for 2D reconstruction problems as it promotes sparsity in the difference of successive coefficients of $\mathbf{x}$ to achieve spatial smoothness. For 2D problems, TV imposes spatial variation sparsity in the horizontal and vertical directions [62], [63].

To apply TV, it is useful to put the unknown vector $\mathbf{x}$ into matrix form with the rows and columns representing the x and y dimensions. Noting the dimensions of the grid are Δd_x and Δd_y, the number of unknowns in each dimension is $N_x = d_x/\Delta d_x$ and $N_y = d_y/\Delta d_y$ respectively, where $N = N_x \times N_y$. Using this form we can reshape the vector $\mathbf{x}$ into the matrix $\mathbf{X} \in \mathbb{R}^{N_x \times N_y}$. Using this notation, the TV objective function can be written in Langrangian form as

$$\min_{\mathbf{x} \in \mathbb{R}^{N \times 1}} \quad ||\mathbf{y} - \boldsymbol{\Psi}\mathbf{x}||_2^2 + \lambda \, f_{TV}(\mathbf{X}), \tag{36}$$

where,

$$f_{TV}(\mathbf{X}) = \sum_{i,j} ||\nabla X_{i,j}||_1, \tag{37}$$

and ∇ denotes the forward finite difference operator (gradient operator) and written as $\nabla = [\nabla_x, \nabla_y]^T$ where

$$\nabla_x X_{i,j} = \begin{cases} X_{i+1,j} - X_{i,j} & \text{if } 1 \leq i < N_x \\ 0 & \text{if } j = N_y \end{cases} \tag{38a}$$

$$\nabla_y X_{i,j} = \begin{cases} X_{i,j+1} - X_{i,j} & \text{if } 1 \leq j < N_y \\ 0 & \text{if } i = N_x. \end{cases} \tag{38b}$$

Hence, (37) can be rewritten as,

$$f_{TV}(\mathbf{X}) = \sum_{i,j} \left(||\nabla_x X_{i,j}||_1 + ||\nabla_y X_{i,j}||_1 \right). \tag{39}$$

Therefore, the TV problem (36) obtains a solution which is sparse in terms of spatial variation (in both horizontal and vertical direction). It can be solved efficiently using algorithms such as the Augmented Lagrangian and Alternative Direction algorithm [62], [63]. The numerical process for solving TV efficiently and selecting the hyper-parameters such as regularization parameters is described in [62].

V. xRPI IMPLEMENTATION SUMMARY

To provide clarity about the integration of all the components of our proposed xRPI formulation, we provide algorithm flowcharts that summarize the steps involved in xRPI. The proposed algorithm is shown in Fig. 4(a). The core of the algorithm is the estimation of sensitivity weight matrix $\boldsymbol{\Psi}$ and the steps involved in its computation are shown in Fig. 4(b).
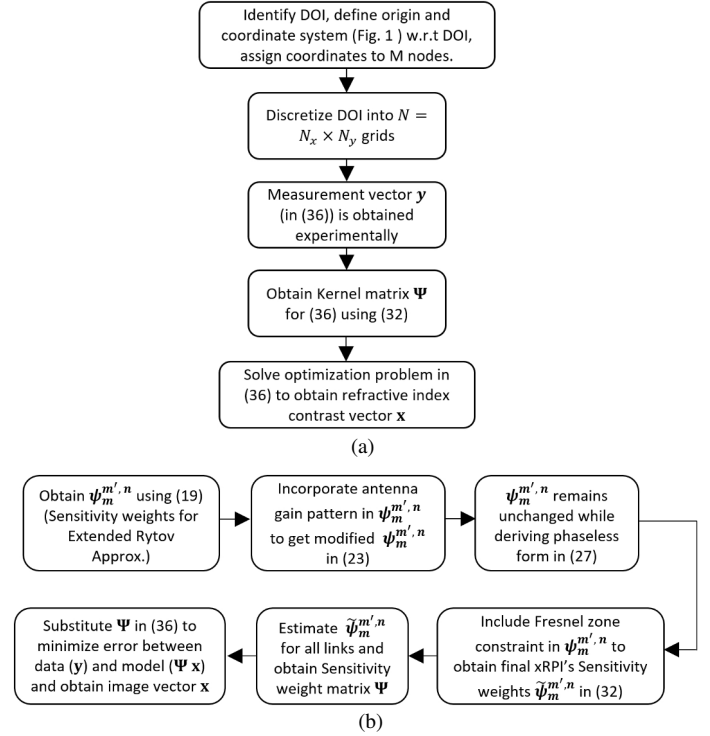

Fig. 4: Flowchart summary of xRPI. (a) Implementation details for overall xRPI algorithm, (b) Details for determining the sensitivity weight matrix $\boldsymbol{\Psi}$ for xRPI.

VI. EXPERIMENTAL CONFIGURATION AND RESULTS

The effectiveness of xRPI (34) is demonstrated with experimental results. The experiments are performed utilizing a WiFi system which is inexpensive and straightforward to use for acquiring RSSI measurements and is described later. To benchmark xRPI, we compare it to RTI which is commonly used for indoor imaging of change in shadowing loss $\Delta\alpha_r(\mathbf{r}_n)$ [20]–[23], [29]. While there are other inverse scattering algorithms for imaging in a wide variety of applications, RTI is the only mainstream approach for performing indoor imaging of change using RSSI measurements of 2.4 GHz WiFi signals when the objects of interest and DOI are larger than λ_0. For clarity of comparison the specific form of RTI we use is also defined. In particular, change in received power $\Delta\mathcal{P}_m(\mathbf{r}_{m'})$ (dB) is related to change in shadowing loss using,

$$\Delta\mathcal{P}_m(\mathbf{r}_{m'}) = \sum_{\forall n | \mathbf{r}_n \in \mathcal{D}} w_m^{m',n} \Delta\alpha_r(\mathbf{r}_n), \tag{40}$$

where the weight matrix utilized is inversely proportional to the square root of the link distance $r_{m,m'}$ and written as

$$w_m^{m',n} = \frac{1}{\sqrt{r_{m,m'}}} \begin{cases} 1 & \text{if } r_{m,n} + r_{n,m'} < r_{m,m'} + \delta \\ 0 & \text{otherwise.} \end{cases} \tag{41}$$

where $r_{m,m'}, r_{m,n}, r_{n,m'}$ are as defined in Fig. 3. Furthermore if the weight falls outside an illumination ellipse defined by δ then it is set to zero. The parameter δ controls the width of the ellipse and is not related to a Fresnel zone and remains constant for any link considered [20]–[23]. There are many variants of RTI which use enhanced optimization methods or hardware [20]–[23], [29], but the core mathematical model of the algorithm remains the same as RTI and is the reason we compare xRPI with (41). We also use the same optimization approach (TV) and same measurement data to solve both xRPI and RTI. This ensures that any improvement in the results is due to the improvement in the model and not other factors.

Comparing RTI (40) with xRPI (34) also highlights the differences in the approaches. RTI is largely heuristically motivated while (34) is formulated directly from the underlying wave equations. The variable α_r in RTI is empirically related to relative attenuation caused by the scatterers and does not represent any physical quantity. This is in contrast to (34) which is related directly to refractive index. For this reason RTI is typically only associated with binary images or localization [20]–[29].

In the next subsections, we provide details of the experimental measurement system, reconstruction quality assessment and experimental results.

A. Experimental System Configuration

The experimental configuration utilizes $M = 20$ WiFi nodes so that there are in total $L = 190$ unique measurement links ($L = M(M-1)/2$). Each node consists of a SparkFun ESP32 Thing board [64] consisting of an integrated 802.11 bgn WiFi transceiver operating at 2.4 GHz. To meet our requirement for the use of directional antennas, the inbuilt omnidirectional antenna of the SparkFun ESP32 boards are replaced by a Yagi antenna of 6.6 dBi as shown in Fig. 5. The Yagi antenna is connected to ESP32 using a soldered Eletro-mechanical connector. For reference, Fig. 6a and Fig. 6b provide gain patterns for the Yagi antenna in the xz-plane (in the DOI plane) and yz plane (normal to the DOI plane) respectively.

The ESP32 boards (with antenna) are located at a height of $d_h = 1.2$ m from the floor using a wooden stand (see Fig. 7a). The antennas on the boards are oriented such that the xz-plane in Fig. 5 lies in the 2D DOI plane and yz-plane (center dipole element of the antenna) is normal to 2D DOI plane and hence matches our TM (vertical polarization) formulations. All nodes are configured to alternate between access point (AP) and station (STA) mode so that the WiFi beacon signal can be utilized to obtain the RSSI for each link. The RSSI measurements from these 20 nodes are collected from the STA by using an external AP that is connected to a server. Acquiring one complete measurement set of 190 measurements takes around 10 sec but in practice the scan speed can be increased. The time between frames Δt is set to one minute in the results that follow.

B. Reconstruction Quality Assessment

There are several metrics to assess the quality of a reconstructed image by comparing it to the ground truth image.
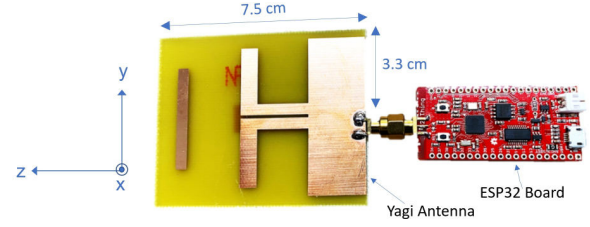

Fig. 5: SparkFun ESP32 Thing board attached with a Yagi antenna. The coordinates system is shown in left. The xz-plane lies in the plane of DOI and yz-plane is normal to DOI plane. The antenna shown on yz-plane consists of three elements namely, director (in left), dipole and balun (in center) and reflector (in right).
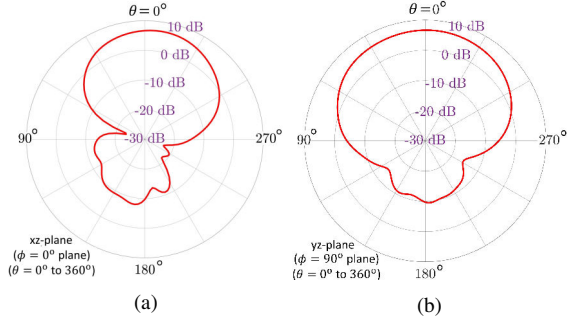

Fig. 6: Gain patterns for the Yagi antenna shown in Fig. 5. (a) Gain pattern in xz-plane (refer to Fig. 5) and (b) Gain pattern in yz-plane.

Common metrics include Relative Error (RE), Mean Square Error (MSE), Peak Signal to Noise Ratio (PSNR) and Structural Similarity Index Measure (SSIM) [65]–[67]. We use both PSNR and SSIM to evaluate the reconstruction performance when we compare our new method, xRPI, with our benchmark, RTI.

In making the comparisons it is important to note again that both RTI and xRPI reconstruct the shape of the scatterer but both methods are estimating different properties of the scatterers. xRPI provides refractive index reconstructions directly related to the material type whereas RTI provides an empirical estimate of the relative attenuation or shadowing. Hence, the image reconstructed using RTI and xRPI will have different scales. Therefore, we normalize the pixel values in both reconstructed images as well as the ground truth image to the range $[0, 1]$ so that a fair comparison can be made between the reconstructed shape and localization accuracy of both techniques. The ground truth image for each experimental setup consists of zero for regions with no temporal change and pixel values of $\Delta\nu(\mathbf{r}_n)$ for regions where objects are placed, after the interval Δt, and then the entire image is normalized to the range $[0, 1]$.

The PSNR between the normalized ground truth image X and reconstructed image Y (both of dimensions $N_x \times N_y$) is defined as:

$$\text{PSNR(dB)} = 10 \log(\frac{I_{peak}^2}{MSE}), \tag{42}$$

where I_{peak} is the maximum pixel value in the image and MSE is mean square error defined as,

$$MSE = \frac{1}{N_x N_y} \sum_{n_x=1}^{N_x} \sum_{n_y=1}^{N_y} ||X(n_x, n_y) - Y(n_x, n_y)||^2. \tag{43}$$

The higher the value of PSNR, the closer is the reconstructed image to the ground truth image.

SSIM is defined as [65], [66],

$$SSIM = \frac{(2\mu_x\mu_y + c_1)(2\sigma_{xy} + c_2)}{(\mu_x^2 + \mu_y^2 + c_1)(\sigma_x^2 + \sigma_y^2 + c_2)}, \quad (44)$$

where, (μ_x, μ_y), (σ_x^2, σ_y^2) and σ_{xy} are the local means, variances, and cross-covariance for images X and Y. The constants c_1 and c_2 are used to make division by small values stable [65]. The value of SSIM lies in the range 0 to 1 and SSIM is equal to 1 if X and Y are the same. Therefore, the closer SSIM is to unity, better is the reconstruction in terms of structural similarity with the ground truth. Further details about the implementation of SSIM can be found in [65]–[67].

C. Experimental Results

Experimental results using our 20 node measurement system are provided for two different DOI. The first results are for a DOI measuring 3×3 m^2 inside a laboratory (Room 3125 at the Hong Kong University of Science and Technology (HKUST)) with a clear area as shown in Fig. 7a. We refer to this DOI configuration as "Clear DOI" in the remaining sections. It can be seen that there is significant clutter outside Clear DOI which could affect measurements inside. The second DOI is for an office environment of size 5×5 m^2 in which there are occluding soft partitions between desks (Room 3116 at HKUST) as shown in Fig. 7b (also shown later in more detail in Fig. 13). We refer to this configuration as "Office DOI" in the remaining sections. It can be seen that in Office DOI (Fig. 7c), objects are occluded by the soft partitions and that there is significant clutter inside as well as outside the DOI (including partition walls, furniture, computers, book shelf).
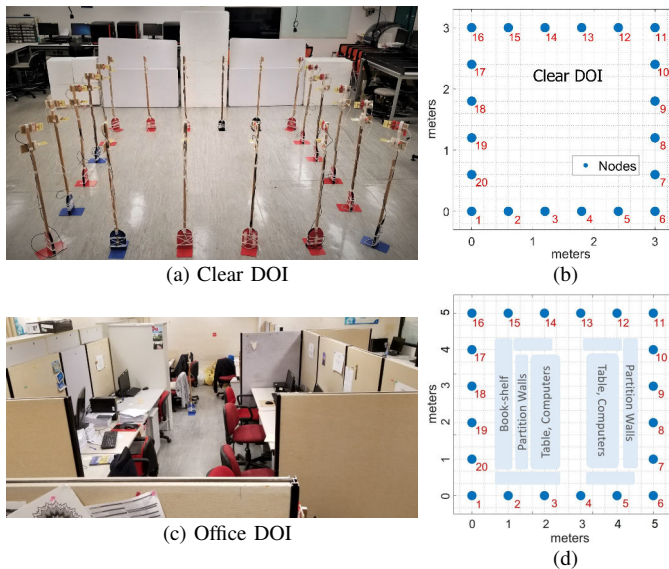

Fig. 7: The two DOI considered. (a) Clear DOI of size 3×3 m^2 in lab 3125 at HKUST. 20 nodes (ESP32 boards with Yagi antenna) are placed around DOI at height 1.2 m from the floor using wooden stands. (b) shows coordinates of the 20 nodes. (c) Office DOI of size 5×5 m^2 in room 3116 at HKUST (more detailed pictures are shown in Fig. 13). (d) Coordinates of the 20 nodes.

Our goal is to test xRPI for low as well as high refractive index objects and for different sizes. To achieve this, we provide results for combinations of three object types, consisting of book stacks (Fig. 8, Fig. 14), a water filled container (Fig. 10 and Fig. 11) and people (Fig. 11 and Fig. 15). The book stacks act as low refractive index objects whereas the human body and water filled container act as medium and high refractive index objects respectively. Table I summarizes the sizes (2D cross sectional area) and refractive index of the test objects used in our experiments. These values are used as reference to test the accuracy of xRPI.

TABLE I: Refractive index and cross sectional area of objects under test. The refractive index of the paper used in book stack was estimated from measurements using a cavity resonator approach. The samples of paper include normal book paper (70 g/m^2) and hard cover (150 g/m^2). The refractive index of water filled container and human body is referenced from [46]–[48].

Test Object	Refractive index $\nu = \sqrt{\epsilon_r}$	Cross section area in DOI plane
Book stack (used in Fig. 8)	$1.67 < \nu^{book} < 1.85$	30×42 cm^2
Book stack (used in Fig. 10, 11)	$1.67 < \nu^{book} < 1.85$	80×30 cm^2
Book stack (used in Fig. 14)	$1.67 < \nu^{book} < 1.85$	45×65 cm^2
Water filled container (used in Fig. 10, 11)	$\nu^{water} = 8.7$	82×45 cm^2
Person (standing in Fig. 11, 15)	$4.5 < \nu^{human} < 7.4$	30×45 cm^2

1) Clear DOI Results: In the first set of experiments, we focus on the Clear DOI with three combinations of our reference objects of book stacks, water filled container and people. In the first set of results, we consider two book stacks at different separations (Fig. 8). In the second set, we consider a stack of books with a container of water (Fig. 10). In the third set, a stack of books, container of water and a person (Fig. 11).

The first object configuration is shown in Fig. 8 where two book stacks are placed inside Clear DOI. Since the 2D DOI plane is at height 1.2 m above ground, we used trolleys as a base so that the book stacks lie in the DOI plane. Reflections from floor, ceiling and trolley are weak due to the directivity of the antennas (Fig. 6b). Furthermore, there are also weak reflections from the surrounding object clutter outside the DOI. These reflections are effectively canceled by using the proposed temporal background subtraction formulation in (34).

To perform the experiment we first acquire measurements $(\mathcal{P}^{t_0})$ at initial time t_0 with only trolleys inside the Clear DOI. At the second time instant (after Δt duration), books are placed on the trolleys to obtain another measurement $(\mathcal{P}^{t_0+\Delta t})$. Subtracting these two measurements gives $(\Delta\mathcal{P})$ and we then use (34) to obtain an image of change in refractive index $\Delta\nu(\mathbf{r}_n) = [\nu^{t_0+\Delta t}(\mathbf{r}_n) - \nu^{t_0}(\mathbf{r}_n)] = \Delta\chi(\mathbf{r}_n)/2$. This change in profile represents the refractive index profile of the books as all other objects are the same across two time instants.

In Fig. 8, the distance (inner edge to inner edge) between the two book stacks is 1.65 m which is 13.2 times the incident wavelength ($\lambda_0 = 12.5$ cm). We denote this distance as $d_0 = 13.2\,\lambda_0$. For reconstruction, we discretize 3×3 m^2 DOI

Fig. 8: Two book stacks inside the Clear DOI. Each book stack has dimensions 30×42 cm^2 and the center of the stacks are at (0.55, 0.6) m and (2.5, 0.6) m. The shortest distance (inner edge to inner edge) between the two stacks is $d_0 = 1.65$ m (or $d_0 = 13.2 \lambda_0$ where, $\lambda_0 = 12.5$ cm). The coordinates of the nodes are as shown in Fig. 7b where the origin is defined at bottom-left corner node.

into grids of area 2×2 cm^2. Therefore, there are $N = 22500$ total unknowns which need to be solved using $L = 190$ measurements and as a result it is a severely underdetermined problem. The use of TV is therefore essential in obtaining a solution as described in section IV.

Fig. 9(a) shows the reconstruction of change in the refractive index profile $\Delta\nu(\mathbf{r}_n)$ using our proposed method, xRPI while Fig. 9(b) provides a reconstruction of the relative attenuation profile $\Delta\alpha_r$ using conventional RTI. It is important to note that the scale in Fig. 9(a) is for $\Delta\nu(\mathbf{r}_n)$ while that for Fig. 9(b) is $\Delta\alpha_r$. The two rectangles shown in dotted green lines in Fig. 9(a) and (b) are the true boundaries of the stacks of books. The SSIM and PSNR values (see Section VI-B for definitions) are also provided in the caption of the reconstructed images.

Fig. 9(a) and (b) clearly show that xRPI provides considerably better reconstruction of shape than RTI. Both PSNR and SSIM values for xRPI are considerably better than RTI. In Fig. 9(a), the change in refractive index at locations of the books is estimated to be $\Delta\nu = 0.7$ (it is the median value of all $\Delta\nu(\mathbf{r}_n)$ values inside the true boundaries of the book stacks) implying that the estimated refractive index of the book stacks is $\nu^{t+\Delta t} = 1 + \Delta\nu = 1.7$. This is within the range of the actual refractive index of the book stacks ($1.67 < \nu^{paper} < 1.85$, see table I). On the other hand, RTI provides relative attenuation or shadowing $\Delta\alpha_r$ which does not directly represent any physical quantity and is high if the object is present and otherwise low.

It can be clearly seen that the proposed xRPI method (Fig. 9(a)) outperforms RTI (Fig. 9(b)) in reconstruction quality. Additionally, xRPI also provides good estimates of refractive index which is not possible with RTI.

Results for when the separations d_0 between the two book stacks are smaller are also provided. Results for $d_0 = 2.4 \lambda_0$ with the center being at (1.3, 0.6) m and (1.9, 0.6) m are shown in Fig. 9(c) and (d) for xRPI and RTI respectively. Results for $d_0 = \lambda_0$ are shown in Fig. 9(e) and (f). xRPI can still distinguish the boundaries between the two stacks whereas these boundaries are now completely indistinguishable in Fig. 9(f) when RTI is used. There is a slight decrease in performance of xRPI as compared to when the distance between the book stacks was larger.

(a) Proposed method.
(SSIM = 0.897, PSNR = 18.2 dB)

(b) RTI.
(SSIM = 0.725, PSNR = 11.4 dB)

(c) Proposed method.
(SSIM = 0.893, PSNR = 16.2 dB)

(d) RTI.
(SSIM = 0.791, PSNR = 11 dB)

(e) Proposed method.
(SSIM = 0.850, PSNR = 13 dB)
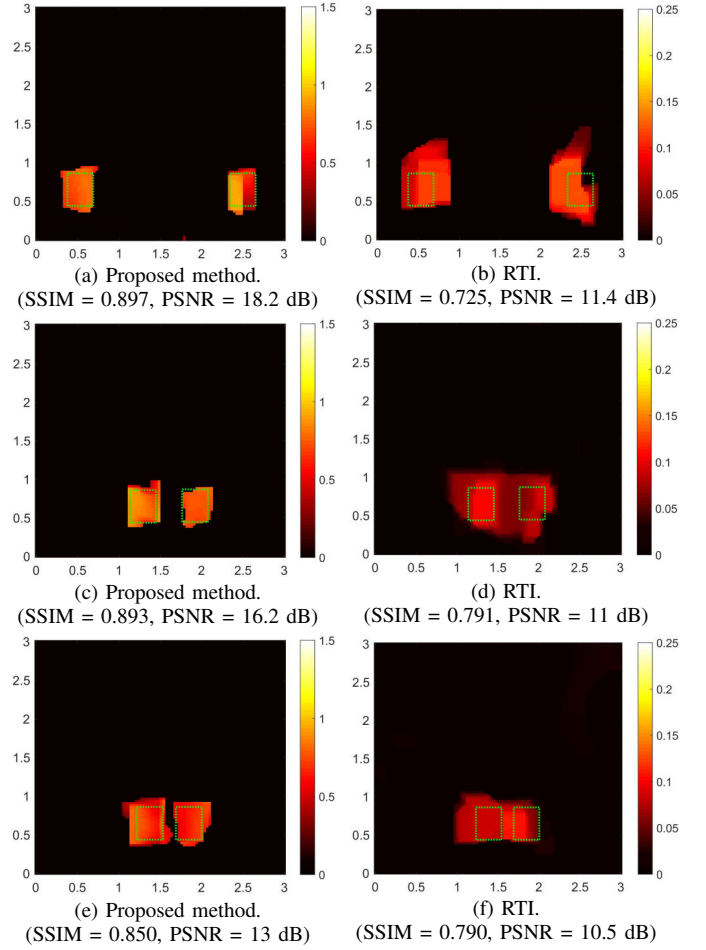
(f) RTI.
(SSIM = 0.790, PSNR = 10.5 dB)

Fig. 9: Imaging results for setup shown in Fig. 8. The results on left ((a), (c) and (e)) are for proposed method xRPI and represents change in refractive index profile ($\nu(\mathbf{r}_n)$). The results on right ((b), (d) and (f)) are for RTI and represents relative attenuation ($\alpha_r(\mathbf{r}_n)$). The two rectangles shown in dotted green lines in all results represent the true boundaries of the book stacks. The SSIM and PSNR values are listed below each reconstructed image to provide comparisons with the ground truth image.

Overall, the results in Fig. 9 show that xRPI can successfully reconstruct the profile of low refractive index objects and can distinguish two objects when their separation is greater than the incident wavelength.

In the next set of experiments, we include a water filled container and a person with the book stacks (see Fig. 10, 11). The objective is to understand the effects of high refractive index objects on reconstruction quality as well as determining whether xRPI can distinguish between high and low refractive index objects.

The first configuration we consider is a book stack and a water filled container as shown in Fig. 10(a). Two tables are again used to provide sufficient height to reach the DOI plane. The centers of the book stack and water container are (1, 2.3) m and (2.3, 0.7) m respectively. Two sets of measurements were taken as in the previous experiment, one at initial time t_0, $\mathcal{P}^{t_0}$ when only tables were present and a second measurement at $t_0 + \Delta t$, $\mathcal{P}^{t_0 + \Delta t}$ when the objects were present too.

Fig. 10(b) and (c) show reconstruction results (along-with the SSIM and PSNR values) for the setup shown in Fig. 10(a) using xRPI ($\Delta\nu(\mathbf{r}_n)$ profile) and RTI ($\Delta\alpha_r(\mathbf{r}_n)$ profile).
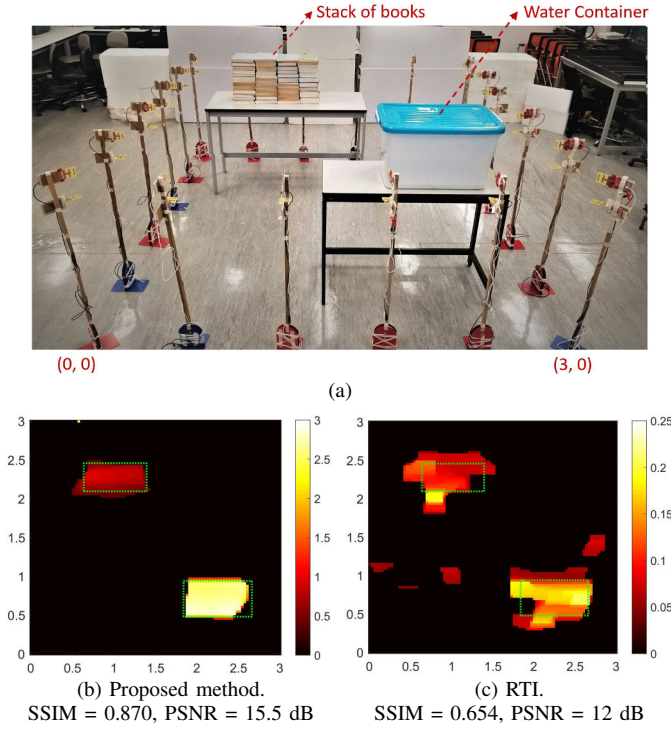
Fig. 10: Clear DOI results for book stack and water filled container. (a) Setup. (b) Reconstruction of change in refractive index profile $(\nu(\mathbf{r}_n))$ using xRPI. (c) Reconstruction of relative attenuation profile $(\alpha_r(\mathbf{r}_n))$ using RTI. The two rectangles shown in dotted green lines in (b) and (c) represent the true boundaries of stack of books and water container. The SSIM and PSNR values are listed below each reconstructed image to provide comparisons with the ground truth image.

The two rectangles with dotted green lines in Fig. 10(b) and (c) show the true boundaries of the objects. Fig. 10(b) and (c) clearly show that xRPI outperforms RTI and provides good reconstruction of the cross section of both objects. More importantly, the reconstructed image in Fig. 10(b) clearly distinguishes between books and water.

The change in refractive index at locations of the water container is estimated to be $\Delta\nu = 2.8$ (median value of all $\Delta\nu(\mathbf{r}_n)$ inside the true boundary of the object) so that the estimated refractive index of water is $\nu^{t+\Delta t} = 1 + \Delta\nu = 3.8$. This is smaller than the actual value ($\nu^{water} = 8.7$, see table I) and is not unexpected. The underestimate is due to the high refractive index of water which violates the assumptions used to derive our linear model (xRPI) and also the underlying extended Rytov approximation. However it is important to note that the proposed method provides good distinction between books and water and the boundaries are still well constructed. The change in refractive index due to water ($\Delta\nu = 2.8$) is 4 times higher than the change in refractive index caused by books ($\Delta\nu = 0.7$). On the other hand, the RTI method not only failed to produce accurate shape reconstructions, it also cannot provide sufficient range to clearly distinguish the water and book objects.

In the next configuration, a book stack, water container, and a person standing inside the DOI at location (1.2, 1) m (see Fig. 11(a)) is utilized. Fig. 11(b) and (c) provide reconstructions of the profile shown in Fig. 11(a) using xRPI
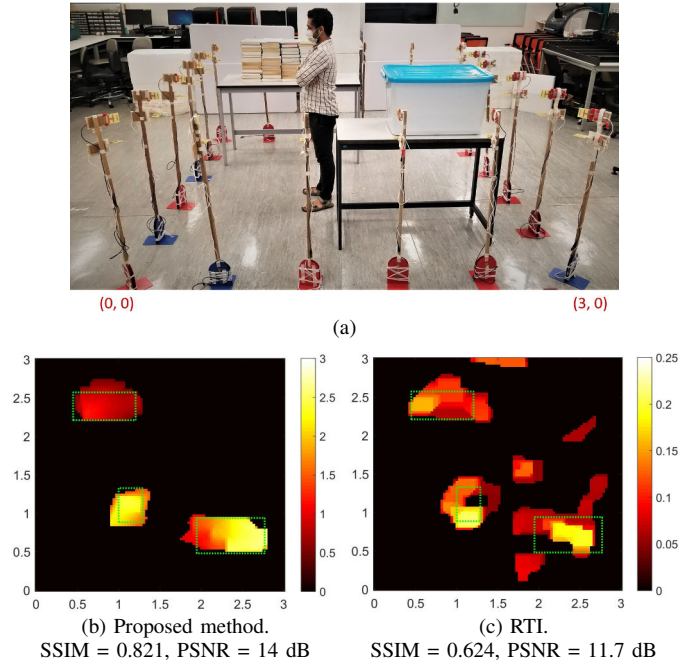

Fig. 11: Clear DOI results for book stack, water filled container and person. (a) Setup (b) Reconstruction of change in refractive index profile $(\nu(\mathbf{r}_n))$ using xRPI. (c) Reconstruction of relative attenuation profile $(\alpha_r(\mathbf{r}_n))$ using RTI. The three rectangles shown in dotted green lines in (b) and (c) represent the true boundaries of the book stacks, water container and person inside DOI. The SSIM and PSNR values are listed below each reconstructed image to provide comparisons with the ground truth image.
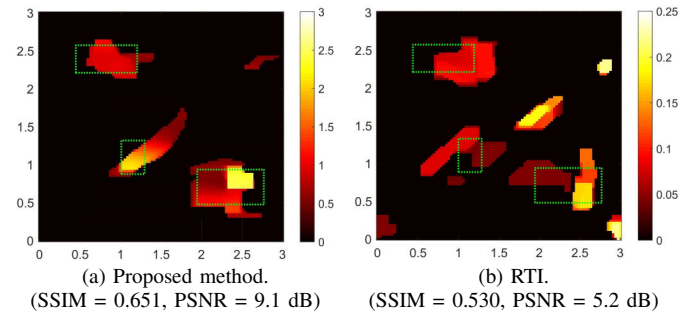

Fig. 12: Reconstruction of profile shown in Fig. 11(a) using 12 nodes instead of 20 nodes (66 measurements instead of 190). (a) Reconstruction of change in refractive index profile $(\nu(\mathbf{r}_n))$ using xRPI. (b) Reconstruction of relative attenuation profile $(\alpha_r(\mathbf{r}_n))$ using RTI.

$(\Delta\nu(\mathbf{r}_n)$ profile) and RTI ($\Delta\alpha_r(\mathbf{r}_n)$ profile) respectively. The true boundaries of the water container, books and human body are shown by the dotted green rectangles in Fig. 11(b) and (c). The rectangle used for the human body is 30×45 cm^2 which is used to represent the typical cross-section area occupied by a human body in DOI. Fig. 11 clearly shows that xRPI again outperforms RTI in reconstruction quality. Furthermore, the proposed method estimates the change in refractive index of the human body to be $\Delta\nu = 2.4$ (median value of all $\Delta\nu(\mathbf{r}_n)$ values inside the dotted rectangular boundary Fig. 11b). That is, the estimated refractive index for the human body using proposed method is $\nu = \Delta\nu + 1 = 3.4$. The estimated value of $\nu = 3.4$ for the human body is smaller than the estimated refractive index of water ($\nu = 3.8$) but more than two times larger than books ($\nu = 1.7$). This again demonstrates that

This article has been accepted for publication in a future issue of this journal, but has not been fully edited. Content may change prior to final publication. Citation information: DOI 10.1109/TVT.2021.3101009, IEEE Transactions on Vehicular Technology

13

the proposed method could distinguish objects with different refractive index which is not possible using RTI.

We also investigated the effect of the number of measurements (number of nodes) on the reconstruction. Fig. 12 shows the reconstruction of the same profile as in Fig. 11 but where we used data from only $M = 12$ nodes instead of 20. The number of measurements $L = M(M-1)/2$ is 66 instead of 190. The number of unknowns are the same as Fig. 11 ($N = 22500$). As expected, due to the decrease in the number of measurements, the inverse problem becomes further underdetermined. Due to this, the reconstruction accuracy decreases. However, the proposed method can still estimate the location of three objects with good accuracy.

(a)

(b)

(c)

Fig. 13: Office DOI. (a) Boundary of the Office DOI using red-dotted quadrilateral which is of dimension 5×5 m^2. 20 nodes are placed along this boundary. The coordinate system is defined in meters (m). (b) and (c) shows the images of DOI shown in (a) from different perspectives.

2) Office DOI Results: In the next set of experiments, we use an indoor environment in which there is clutter both inside and outside the DOI (see Fig. 13). Inside the DOI there are 9 cubicles including a wide range of objects such as computers, desks, chairs and cubicle walls. One whole side of the DOI (from (0,0) to (0,5)) is obstructed with a large book shelf made up of wood that is filled with books (see Fig. 13(a) and (c)). The other 3 sides are obstructed with cubicle walls which are

made up of wood, steel and aluminum frames and medium-density fibreboard (MDF). The book shelves and cubicle walls form a closed area in the DOI with a narrow walkway space as shown in Fig. 13(b).

To test xRPI in this cluttered DOI, we placed a book stack on a trolley inside the DOI as shown in Fig. 14(a). The center of this stack lies at location (2.8, 4) m with dimensions 45×65 cm^2. Fig. 14(b) and (c) provides reconstructions using xRPI ($\Delta \nu(\mathbf{r}_n)$ profile) and RTI ($\Delta \alpha_r(\mathbf{r}_n)$ profile) respectively. It can be clearly seen that xRPI efficiently removes the clutter. The estimated refractive index of the books is found to be $\nu = (\Delta \nu + 1) = 1.65$ and agrees well with the previous experimental results of 1.7.
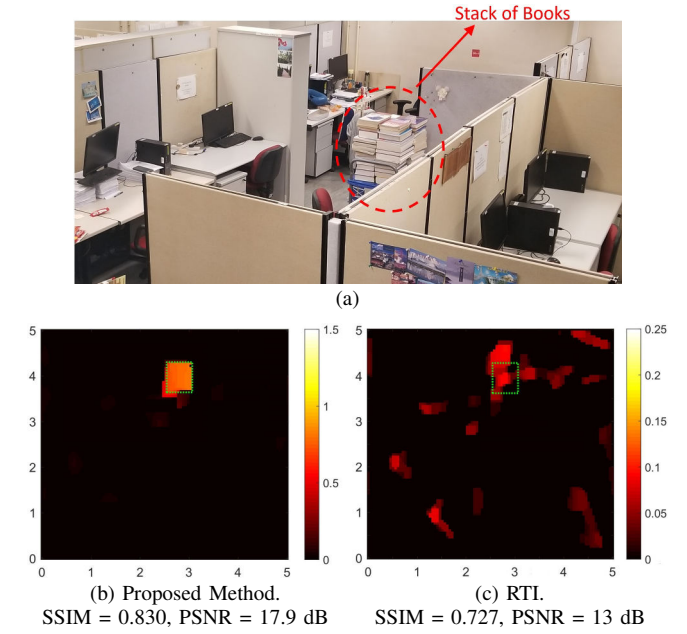

(a)

(b) Proposed Method.
SSIM = 0.830, PSNR = 17.9 dB

(c) RTI.
SSIM = 0.727, PSNR = 13 dB

Fig. 14: Office DOI with a book stack. (a) Setup. (b) Reconstruction of change in refractive index profile ($\nu(\mathbf{r}_n)$) using xRPI. (c) shows change in relative attenuation profile ($\alpha_r(\mathbf{r}_n)$) using RTI. The rectangle shown in dotted green lines in (b) and (c) represent the true boundary of the stack of books. The SSIM and PSNR values are listed below each reconstructed image to provide comparisons with the ground truth image.

In the next experiment, a person is standing at (2, 1.9) m (Fig. 15(a)). Fig. 15(b) and (c) show again that xRPI provides significantly better reconstructions than RTI. The estimated refractive index of the human body is found to be 3.4, again agreeing with the previous experiment in the Clear DOI.

In all configurations xRPI outperforms RTI in the reconstruction of shape and in addition provides an estimate of refractive index. To the best of our knowledge, xRPI is the first WiFi based indoor imaging framework to demonstrate accurate imaging of objects of different refractive indices while also providing approximate estimates of refractive index.

VII. CONCLUSIONS AND FUTURE WORK

The problem of device free localization and imaging within an indoor environment using an inverse scattering perspective has been considered. A new method, xRPI, for imaging temporal change in refractive index using WiFi RSSI measurements is introduced. The method is based on a new extended
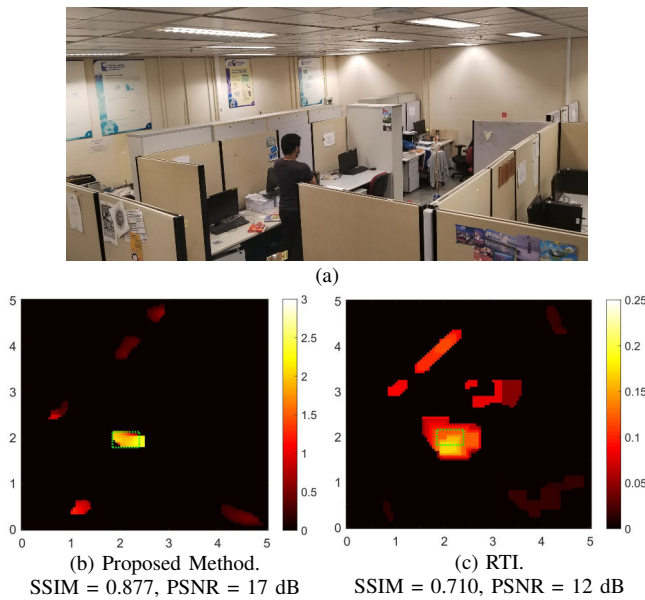
This article has been accepted for publication in a future issue of this journal, but has not been fully edited. Content may change prior to final publication. Citation information: DOI 10.1109/TVT.2021.3101009, IEEE Transactions on Vehicular Technology

14

(a)

(b) Proposed Method.
SSIM = 0.877, PSNR = 17 dB

(c) RTI.
SSIM = 0.710, PSNR = 12 dB

Fig. 15: Office DOI with a person. (a) Setup. (b) Reconstruction of change in refractive index profile $(\nu(\mathbf{r}_n))$ using xRPI. (c) Reconstruction of relative attenuation profile $(\alpha_r(\mathbf{r}_n))$ using RTI. The rectangle shown in dotted green lines in (b) and (c) represent the true boundary of area occupied by the person. The SSIM and PSNR values are listed below each reconstructed image to provide comparisons with the ground truth image.

Rytov phaseless imaging formulation that includes a ray based high frequency approximation to the total field, a phaseless RSSI formulation, temporal background subtraction, directive antennas and Fresnel zones. In addition, methods to reduce the number of RSSI measurements required for indoor imaging are also presented and these use a strong spatial sparsity constraint and this directly results from imaging change in the environment.

Reconstruction results of xRPI were provided using a wide range of experiments and compared with a benchmark based on RTI. The experiments were conducted in indoor environments which include occlusion, clutter and obstructions. The experimental results show that the proposed method provides considerably better reconstruction performance than conventional RTI. Apart from accurate shape reconstruction, the proposed method also provides approximate estimates of refractive index which has not been performed by RTI or any other indoor RF imaging techniques. Refractive index estimation is very useful for distinguishing different materials, such as wood and people, in the DOI.

Scope for future work includes further improvement of the Rytov approximation so that it can handle high refractive index objects such as water more accurately. In addition, extensions that include some of the possible 3D propagation effects would also be worth considering. Another aspect to consider is enhanced hardware which can acquire measurements more quickly. This can help in achieving a real-time imaging system.

Acknowledgments

References

[1] D. Sato, U. Oh, K. Naito, H. Takagi, K. Kitani, and C. Asakawa, "NavCog3: An evaluation of a smartphone-based blind indoor navigation assistant with semantic features in a large-scale environment," in *Proceedings of the 19th International ACM SIGACCESS Conference on Computers and Accessibility*, 2017, pp. 270–279.

[2] F. Guidi, A. Mariani, A. Guerra, D. Dardari, A. Clemente, and R. D'Errico, "Indoor environment-adaptive mapping with beamsteering massive arrays," *IEEE Transactions on Vehicular Technology*, vol. 67, no. 10, pp. 10 139–10 143, 2018.

[3] H. Liu, H. Darabi, P. Banerjee, and J. Liu, "Survey of wireless indoor positioning techniques and systems," *IEEE Transactions on Systems, Man, and Cybernetics, Part C (Applications and Reviews)*, vol. 37, no. 6, pp. 1067–1080, 2007.

[4] D. Pastina, F. Colone, T. Martelli, and P. Falcone, "Parasitic exploitation of WiFi signals for indoor radar surveillance," *IEEE Transactions on Vehicular Technology*, vol. 64, no. 4, pp. 1401–1415, 2015.

[5] L. Zhang, Q. Gao, X. Ma, J. Wang, T. Yang, and H. Wang, "DeFi: Robust training-free device-free wireless localization with WiFi," *IEEE Transactions on Vehicular Technology*, vol. 67, no. 9, pp. 8822–8831, 2018.

[6] J. Hong and T. Ohtsuki, "Signal eigenvector-based device-free passive localization using array sensor," *IEEE Transactions on Vehicular Technology*, vol. 64, no. 4, pp. 1354–1363, 2015.

[7] K. Chetty, G. E. Smith, and K. Woodbridge, "Through-the-wall sensing of personnel using passive bistatic WiFi radar at standoff distances," *IEEE Transactions on Geoscience and Remote Sensing*, vol. 50, no. 4, pp. 1218–1226, 2011.

[8] X. Sun, X. Gao, G. Y. Li, and W. Han, "Single-site localization based on a new type of fingerprint for massive MIMO-OFDM systems," *IEEE Transactions on Vehicular Technology*, vol. 67, no. 7, pp. 6134–6145, 2018.

[9] B. Liu, A. P. Guevara, S. De Bast, Q. Wang, and S. Pollin, "Massive MIMO indoor localization with 64-antenna uniform linear array," in *2020 IEEE 91st Vehicular Technology Conference (VTC2020-Spring)*. IEEE, 2020, pp. 1–5.

[10] W. Zhang and A. Hoorfar, "A generalized approach for SAR and MIMO radar imaging of building interior targets with compressive sensing," *IEEE Antennas and Wireless Propagation Letters*, vol. 14, pp. 1052–1055, 2015.

[11] Z. Kong and Q. Lu, "A brief review of simultaneous localization and mapping," in *IECON 2017-43rd Annual Conference of the IEEE Industrial Electronics Society*. IEEE, 2017, pp. 5517–5522.

[12] Y. Xu, Y. S. Shmaliy, Y. Li, X. Chen, and H. Guo, "Indoor INS/LiDAR-based robot localization with improved robustness using cascaded FIR filter," *IEEE Access*, vol. 7, pp. 34 189–34 197, 2019.

[13] J. Eckert, R. German, and F. Dressler, "An indoor localization framework for four-rotor flying robots using low-power sensor nodes," *IEEE Transactions on Instrumentation and Measurement*, vol. 60, no. 2, pp. 336–344, 2011.

[14] D. Tsai and S. Lai, "Independent component analysis-based background subtraction for indoor surveillance," *IEEE Transactions on Image Processing*, vol. 18, no. 1, pp. 158–167, 2009.

[15] F. Adib and D. Katabi, "See through walls with WiFi!" in *Proceedings of the ACM SIGCOMM 2013 Conference on SIGCOMM*, 2013, pp. 75–86.

[16] F. Adib, Z. Kabelac, and D. Katabi, "Multi-person localization via RF body reflections," in *12th {USENIX} Symposium on Networked Systems Design and Implementation ({NSDI} 15)*, 2015, pp. 279–292.

[17] X. Guo and N. Ansari, "Localization by fusing a group of fingerprints via multiple antennas in indoor environment," *IEEE Transactions on Vehicular Technology*, vol. 66, no. 11, pp. 9904–9915, 2017.

[18] X. Wang, L. Gao, S. Mao, and S. Pandey, "CSI-based fingerprinting for indoor localization: A deep learning approach," *IEEE Transactions on Vehicular Technology*, vol. 66, no. 1, pp. 763–776, 2017.

[19] S. Shi, S. Sigg, L. Chen, and Y. Ji, "Accurate location tracking from CSI-based passive device-free probabilistic fingerprinting," *IEEE Transactions on Vehicular Technology*, vol. 67, no. 6, pp. 5217–5230, 2018.

[20] J. Wilson and N. Patwari, "Radio tomographic imaging with wireless networks," *IEEE Transactions on Mobile Computing*, vol. 9, no. 5, pp. 621–632, 2010.

[21] O. Kaltiokallio, M. Bocca, and N. Patwari, "A fade level-based spatial model for radio tomographic imaging," *IEEE Transactions on Mobile Computing*, vol. 13, no. 6, pp. 1159–1172, 2014.

[22] O. Kaltiokallio, R. Jäntti, and N. Patwari, "ARTI: An adaptive radio tomographic imaging system," *IEEE Transactions on Vehicular Technology*, vol. 66, no. 8, pp. 7302–7316, 2017.

[23] B. Wei, A. Varshney, N. Patwari, W. Hu, T. Voigt, and C. T. Chou, "dRTI: Directional radio tomographic imaging," in *Proceedings of the 14th International Conference on Information Processing in Sensor Networks (IPSN)*, 2015, pp. 166–177.

[24] Y. Zhao, N. Patwari, J. M. Phillips, and S. Venkatasubramanian, "Radio tomographic imaging and tracking of stationary and moving people via kernel distance," in *2013 ACM/IEEE International Conference on Information Processing in Sensor Networks (IPSN)*, 2013, pp. 229–240.

[25] J. Wang, Q. Gao, M. Pan, X. Zhang, Y. Yu, and H. Wang, "Toward accurate device-free wireless localization with a saddle surface model," *IEEE Transactions on Vehicular Technology*, vol. 65, no. 8, pp. 6665–6677, 2016.

[26] S. Savazzi, M. Nicoli, F. Carminati, and M. Riva, "A bayesian approach to device-free localization: Modeling and experimental assessment," *IEEE Journal of Selected Topics in Signal Processing*, vol. 8, no. 1, pp. 16–29, 2014.

[27] J. Wang, X. Zhang, Q. Gao, X. Ma, X. Feng, and H. Wang, "Device-free simultaneous wireless localization and activity recognition with wavelet feature," *IEEE Transactions on Vehicular Technology*, vol. 66, no. 2, pp. 1659–1669, 2017.

[28] Q. Wang, H. Yiğitler, R. Jäntti, and X. Huang, "Localizing multiple objects using radio tomographic imaging technology," *IEEE Transactions on Vehicular Technology*, vol. 65, no. 5, pp. 3641–3656, 2016.

[29] S. Tomic, M. Beko, and R. Dinis, "RSS-based localization in wireless sensor networks using convex relaxation: Noncooperative and cooperative schemes," *IEEE Transactions on Vehicular Technology*, vol. 64, no. 5, pp. 2037–2050, 2015.

[30] S. Depatla, C. R. Karanam, and Y. Mostofi, "Robotic through-wall imaging: Radio-frequency imaging possibilities with unmanned vehicles." *IEEE Antennas and Propagation Magazine*, vol. 59, no. 5, pp. 47–60, 2017.

[31] A. Gonzalez-Ruiz, A. Ghaffarkhah, and Y. Mostofi, "An integrated framework for obstacle mapping with see-through capabilities using laser and wireless channel measurements," *IEEE Sensors Journal*, vol. 14, no. 1, pp. 25–38, 2014.

[32] S. Depatla, L. Buckland, and Y. Mostofi, "X-ray vision with only WiFi power measurements using rytov wave models," *IEEE Transactions on Vehicular Technology*, vol. 64, no. 4, pp. 1376–1387, 2015.

[33] F. Guidi, A. Guerra, and D. Dardari, "Millimeter-wave massive arrays for indoor SLAM," in *2014 IEEE International Conference on Communications Workshops (ICC)*, 2014, pp. 114–120.

[34] E. Jose and M. D. Adams, "An augmented state SLAM formulation for multiple line-of-sight features with millimetre wave radar," in *2005 IEEE/RSJ International Conference on Intelligent Robots and Systems*, 2005, pp. 3087–3092.

[35] A. Rahman, T. Li, and Y. Wang, "Recent advances in indoor localization via visible lights: A survey," *Sensors*, vol. 20, no. 5, p. 1382, 2020.

[36] A. Zayets and E. Steinbach, "Robust WiFi-based indoor localization using multipath component analysis," in *2017 International Conference on Indoor Positioning and Indoor Navigation (IPIN)*, 2017, pp. 1–8.

[37] K. Witrisal, P. Meissner, E. Leitinger, Y. Shen, C. Gustafson, F. Tufvesson, K. Haneda, D. Dardari, A. F. Molisch, A. Conti, and M. Z. Win, "High-accuracy localization for assisted living: 5G systems will turn multipath channels from foe to friend," *IEEE Signal Processing Magazine*, vol. 33, no. 2, pp. 59–70, 2016.

[38] T. Lu, K. Agarwal, Y. Zhong, and X. Chen, "Through-wall imaging: Application of subspace-based optimization method," *Progress In Electromagnetics Research*, vol. 102, pp. 351–366, 2010.

[39] X. Chen, *Computational methods for electromagnetic inverse scattering*. Wiley Online Library, 2018.

[40] R. Bates, V. Smith, and R. D. Murch, "Manageable multidimensional inverse scattering theory," *Physics Reports*, vol. 201, no. 4, pp. 185–277, 1991.

[41] G. Tearney, M. Brezinski, J. Southern, B. Bouma, M. Hee, and J. Fujimoto, "Determination of the refractive index of highly scattering human tissue by optical coherence tomography," *Optics Letters*, vol. 20, no. 21, pp. 2258–2260, 1995.

[42] H. Liu, H. Zhong, N. Karpowicz, Y. Chen, and X. Zhang, "Terahertz spectroscopy and imaging for defense and security applications," *Proceedings of the IEEE*, vol. 95, no. 8, pp. 1514–1527, 2007.

[43] A. Abubakar, T. Habashy, V. Druskin, L. Knizhnerman, and D. Alumbaugh, "2.5D forward and inverse modeling for interpreting low-frequency electromagnetic measurements," *Geophysics*, vol. 73, no. 4, pp. F165–F177, 2008.

[44] R. Zoughi, *Microwave non-destructive testing and evaluation principles*. Springer Science & Business Media, 2000, vol. 4.

[45] P. Sood, A. Dubey, C. Y. Chiu, and R. Murch, "Demonstrating device-free localization based on radio tomographic imaging," in *2020 IEEE International Symposium on Antennas and Propagation and North American Radio Science Meeting*, 2020, pp. 1227–1228.

[46] K. C. Yaw, "Measurement of dielectric material properties," *Application Note. Rohde & Schwarz*, pp. 1–35, 2012.

[47] E. Aguirre, J. Arpón, L. Azpilicueta, V. Ramos, and F. J. Falcone, "Evaluation of electromagnetic dosimetry of wireless systems in complex indoor scenarios with human body interaction," *Progress In Electromagnetics Research B, Vol. 43, 189-209, 2012.*, 2012.

[48] V. Komarov, S. Wang, and J. Tang, "Permittivity and measurements," *Encyclopedia of RF and Microwave Engineering*, 2005.

[49] A. Dubey, W. Wang, and R. Murch, "Transmission line fault imaging using phaseless inverse scattering and temporal sparsity," *IEEE Transactions on Microwave Theory and Techniques*, vol. 69, no. 1, pp. 284–296, 2021.

[50] P. Müller, M. Schürmann, S. Girardo, G. Cojoc, and J. Guck, "Accurate evaluation of size and refractive index for spherical objects in quantitative phase imaging," *Optics Express*, vol. 26, no. 8, pp. 10 729–10 743, 2018.

[51] Kwok-Wai Cheung, J. H. . Sau, and R. D. Murch, "A new empirical model for indoor propagation prediction," *IEEE Transactions on Vehicular Technology*, vol. 47, no. 3, pp. 996–1001, 1998.

[52] S. Caorsi, A. Massa, and M. Pastorino, "Rytov approximation: application to scattering by two-dimensional weakly nonlinear dielectrics," *JOSA A*, vol. 13, no. 3, pp. 509–516, 1996.

[53] R. D. Murch, "Inverse scattering and shape reconstruction." Ph.D. dissertation, University of Canterbury. Electrical and Electronic Engineering, Canterbury, New Zealand, 1990.

[54] D. S. Jones, "Acoustic and electromagnetic waves," *Oxford/New York, Clarendon Press/Oxford University Press, 1986, 764 p.*, 1986.

[55] K. Zhang, Z. Yin, Z.-C. Li, and Y.-R. Chen, "Wave equation tomographic velocity inversion method based on the Born/Rytov approximation," *Applied Geophysics*, vol. 10, no. 3, pp. 314–322, 2013.

[56] R. Bates, W. Boerner, and G. Dunlop, "An extended Rytov approximation and its significance for remote sensing and inverse scattering," *Optics Communications*, vol. 18, no. 4, pp. 421–423, 1976.

[57] R. E. Collin, *Antennas and radiowave propagation*. McGraw-Hill, 1985.

[58] Y. Zhou, F. Dahlen, and G. Nolet, "Three-dimensional sensitivity kernels for surface wave observables," *Geophysical Journal International*, vol. 158, no. 1, pp. 142–168, 2004.

[59] J. Spetzler and R. Snieder, "The fresnel volume and transmitted waves," *Geophysics*, vol. 69, no. 3, pp. 653–663, 2004.

[60] A. Sieminski, J.-J. Lévêque, and E. Debayle, "Can finite-frequency effects be accounted for in ray theory surface wave tomography?" *Geophysical Research Letters*, vol. 31, no. 24, 2004.

[61] T. S. Rappaport *et al.*, *Wireless communications: principles and practice*. Prentice Hall PTR New Jersey, 1996, vol. 2.

[62] C. Li, W. Yin, and Y. Zhang, "User's guide for TVAL3: TV minimization by augmented lagrangian and alternating direction algorithms," *CAAM Report*, vol. 20, no. 46-47, p. 4, 2009.

[63] C. Li, "Compressive sensing for 3D data processing tasks: applications, models and algorithms," Tech. Rep., 2011.

[64] S. Espressif, "ESP32 datasheet," 2016. [Online]. Available: https://www.sparkfun.com/products/13907

[65] Zhou Wang, A. C. Bovik, H. R. Sheikh, and E. P. Simoncelli, "Image quality assessment: from error visibility to structural similarity," *IEEE Transactions on Image Processing*, vol. 13, no. 4, pp. 600–612, 2004.

[66] U. Sara, M. Akter, and M. S. Uddin, "Image quality assessment through FSIM, SSIM, MSE and PSNR—a comparative study," *Journal of Computer and Communications*, vol. 7, no. 3, pp. 8–18, 2019.

[67] MATLAB R2020a, "Image quality metrics , image processing toolbox," 2014. [Online]. Available: https://www.mathworks.com/help/images/image-quality-metrics.html

This article has been accepted for publication in a future issue of this journal, but has not been fully edited. Content may change prior to final publication. Citation information: DOI 10.1109/TVT.2021.3101009, IEEE Transactions on Vehicular Technology

16

Amartansh Dubey (Graduate Student Member, IEEE) received the MPhil degree in electronic and computer engineering from the Hong Kong University of Science and Technology (HKUST), Hong Kong, in 2018. He is currently pursuing the Ph.D. degree from HKUST. He received the bachelor's degree in electronics and communication engineering from Visvesvaraya National Institute of Technology, Nagpur, India, in 2016.

His research interests include inverse scattering problems, indoor imaging using Wi-Fi signals, statistical signal processing and computational electromagnetics.

Pranay Sood (Student Member, IEEE) received the bachelor's degree in electronic engineering with minors in business and entrepreneurship from The Hong Kong University of Science and Technology (HKUST), Hong Kong in 2018, and the M.Phil. degree in electronic and computer engineering from HKUST in 2020.

His research interests include inverse scattering problems, indoor imaging using Wi-Fi signals, statistical learning, signal processing, applications of machine and deep learning, fintech and healthtech.

Jehiel Santos (Student Member, IEEE) received the B.Sc. degree in Electronics Engineering from University of Santo Tomas, Manila, Philippines, in 2015, and the M.Phil. degree in Electronic and Computer Engineering from The Hong Kong University of Science and Technology (HKUST), Hong Kong, in 2020.

His research interests include one dimensional imaging in transmission lines and signal processing.

Dingfei Ma (Student Member, IEEE) received the B.E. degree from the Harbin Institute of Technology, Harbin, China, in 2017, and the joint M.Sc. degree from the Southern University of Science and Technology (SUSTech), Shenzhen, China, and the Harbin Institute of Technology, in 2019. She is currently pursuing the Ph.D. degree at the Hong Kong University of Science and Technology, Hong Kong.

Her research interests are focused on electromagnetic compressive imaging based on leaky-wave structures.

Chi-Yuk Chiu u (Senior Member, IEEE) received the B.Eng. and M.Eng. degrees and the Ph.D. degree in electronic engineering from the City University of Hong Kong, in 2001, 2001, and 2005, respectively. He joined as a Research Assistant Professor the Department of Electronic and Computer Engineering (ECE), The Hong Kong University of Science and Technology (HKUST) in 2005. He was a Senior Antenna Engineer with Sony Mobile Communications, Beijing, in 2011. He joined as a Research Assistant Professor with the Department of ECE, HKUST, in 2015. He has authored or coauthored 84 articles and two book chapters. He holds several patents related to antenna technology. His main research interests include the design and analysis of small antennas, MIMO antennas, applications of characteristic modes, and energy harvesting. He is also a member of the IEEE Antennas and Propagation Society Education Committee.

Ross Murch (S'84-M'90-SM'98-F'09) received his Bachelor's and Ph.D. degrees in Electrical and Electronic Engineering from the University of Canterbury, New Zealand.

He is currently a Chair Professor in the Department of Electronic and Computer Engineering and a Senior Fellow at the Institute of Advanced Study both at the Hong Kong University of Science and Technology (HKUST). His current research interests include Internet-of-Things, RF imaging, ambient RF systems, multiport antenna systems, reconfigurable intelligent surfaces and acoustics and his unique expertise lies in his combination of knowledge from both wireless communication systems and electromagnetic areas. His research contributions include more than 200 publications and 20 patents on wireless communication systems and antennas and these have attracted over 15,000 citations.

He was Department Head at HKUST from 2009-2015, is an IEEE Fellow and has won several awards including the Computer Simulation Technology (CST) University Publication Award in 2015. He has served IEEE in various positions including area editor, technical program chair, distinguished lecturer and Fellow evaluation committee. He enjoys teaching and has won two teaching awards.